International Journal of Multiphase Flow 174 (2024) 104795

Contents lists available at ScienceDirect

International Journal of Multiphase Flow

journal homepage: www.elsevier.com/locate/ijmulflow

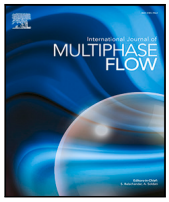

Large-eddy simulation of elliptic hydrofoil tip vortex cavitation under incipient conditions

Filipe L. Brandao [a], Praveen Kumar [a], Krishnan Mahesh [b,*]

[a] University of Minnesota, Aerospace Engineering & Mechanics, USA
[b] University of Michigan, Naval Architecture and Marine Engineering, USA

ARTICLE INFO

Keywords:
Tip vortex cavitation
Large eddy simulation
Confinement

ABSTRACT

Large-eddy simulation (LES) is used to simulate flow over a three-dimensional elliptical hydrofoil at 12 degrees angle of attack and Reynolds numbers (Re) of 9×10^5 and 1.4×10^6 based on root chord length and freestream velocity. The simulations are performed at the cavitation number (σ) of 2.1 and are based on the experiments of Boulon et al. (1999), who studied the tip vortex cavitation behavior under the confinement of side and bottom walls. The present simulations correspond to their case where the confinement due to the bottom wall is negligible. The computational model of Brandao and Mahesh (2022) that treats vapor as a passive scalar in an incompressible liquid is extended to account for multiple groups of bubbles of different sizes, effectively making it a polydisperse model. This allows us to investigate the effects of water quality on inception. The simulations include two different freestream nuclei distributions that are taken from the water tunnel data of Khoo et al. (2020c). It was found that inception is strongly dependent on the amounts of nuclei in the freestream. When the flow is depleted of nuclei, inception is an intermittent event confined to a location very close to the hydrofoil tip. However, when the flow is rich in nuclei, a larger portion of the tip vortex cavitates, as well as part of the suction side very close to the leading edge of the hydrofoil. Probability density functions revealed that cavitation occurs in any region experiencing a pressure field lower than vapor pressure when the flow is rich in nuclei, while extremely low values of pressure (usually kPa of tension) are required to make a flow depleted of nuclei cavitate. The topology of a flow poor in nuclei was investigated and inception was found to occur in regions dominated by irrotational straining with high stretching rates. Lagrangian statistics showed that as Re is increased, nuclei have higher likelihood of experiencing very low pressure fields. However, the amount of time they are subject to very low pressures is also shorter with increasing Re.

1. Introduction

The transverse flow caused by the pressure difference between the pressure and suction sides of a finite-span wing/blade, winds around its tip to form the so-called tip vortex, which is attached to the vortex sheet formed by the vortex shedding along the span of the wing/blade. Moore (1974) suggested that a finite vortex sheet with a tip vortex at its end undergoes a spiral roll-up as it evolves downstream. This in turn entrains some vorticity in the tip vortex, causing an instantaneous change in the velocity field at the locations of other vortices. These perturbations lead to the Kelvin–Helmholtz instability in the region between the tip vortex and the unstretched part of the vortex sheet. Once the roll-up is complete, the tip vortex evolves further downstream in a complex manner depending on the physical conditions and geometry of the problem.

Depending on the roll-up process in the near field, the pressure in the tip vortex core can drop below vapor pressure making it susceptible to cavitation. Cavitation can occur at different scales, starting from inception and ending in developed cavitation, and it is characterized by the cavitation number σ (defined as $\sigma = \frac{p_r - p_v}{0.5\rho u_r^2}$, where p_r, p_v, ρ and u_r are a reference pressure, the vapor pressure, the liquid density and a reference velocity, respectively). It can cause material damage, noise and performance degradation in marine propellers and hence is of prime interest. Following the pioneering work of McCormick (1962), tip vortex cavitation (TVC) has been widely studied in the past as reviewed by Arndt (2002). With the goal of understanding tip vortex cavitation in marine propellers, many past studies simplified the problem and studied the tip vortices generated by fixed hydrofoils (Fruman et al., 1995; Pichon et al., 1997; Boulon et al., 1999; Astolfi et al., 1999; Amini et al., 2019). Arndt et al. (1991) observed that the cavitation number associated with the inception of the tip vortex has a complex dependence on the Reynolds number and on

* Corresponding author.
E-mail address: krmahesh@umich.edu (K. Mahesh).

https://doi.org/10.1016/j.ijmultiphaseflow.2024.104795
Received 17 October 2023; Received in revised form 29 February 2024; Accepted 4 March 2024
Available online 7 March 2024

the water quality (population of bubbles in the freestream). Arndt and Keller (1992), through visual detection, observed that inception in tip vortices would start at higher σ for "weak" water (water where the tensile strength was reduced by the presence of a large number of bubbles). Interestingly, Khoo et al. (2020b) found that the desinence of cavitation (disappearance of cavitation by slowly increasing σ) is largely independent of the nuclei population. Boulon et al. (1999) studied confined flow over a three-dimensional elliptical hydrofoil NACA 16-020. The flow was confined by the presence of fixed side-walls in their water tunnel as well as by an adjustable flat bottom wall, which could be moved in their experiments to achieve a desirable tip gap (e). They found that as e becomes smaller, the tip vortex becomes more susceptible to cavitation up to a certain value of e due to increase in the peak of swirl velocity. Beyond that, decreasing e does not cavitate the flow. Asnaghi et al. (2020) performed numerical simulations of a NACA 66(2)-415 and found that cavitation increases the tip vortex diameter. Xie et al. (2021) investigated cavitation of the tip vortex from a NACA 16-020 elliptic hydrofoil and found that cavitation promotes the production of vorticity and increases the boundary layer thickness. Shin et al. (2021) compared cavitation characteristics over two different hydrofoils: NACA 16-020 and NACA 66(2)-415. They suggest that the development process of TVC, including inception, occurs in six different stages, with decreasing σ.

Simulating tip vortex behind hydrofoils has two major challenges: (i) flow over the hydrofoil surface and (ii) the tip vortex interactions with walls. Flow over the hydrofoil is computationally challenging due to high Re which demands fine resolution near wall to capture boundary layers. Depending on the physical conditions such as Re and angle of attack, the flow on the hydrofoil can be laminar or transitional, and it can separate on the suction side of the hydrofoil causing large unsteadiness. The unsteadiness can be enhanced further if the flow is confined. The tip vortex has a tiny core which needs to be resolved throughout the length of the simulation domain. Maintaining grid quality becomes challenging at small tip gaps. The turbulence in the wake decays moving downstream. Thus, this problem demands an accurate and robust numerical method to capture the essential flow features. Therefore, large eddy simulation (LES) is commonly used to simulate this problem due to its predictive capability, which has been demonstrated in literature for a variety of complex marine flow problems (Mahesh et al., 2015). LES has been also used in past to study the effect of tip-gap on the flow field in a turbomachinery cascade (e.g. You et al., 2006). Mahesh et al. (2004) developed a non-dissipative and robust finite volume method suitable for LES of turbulent flows on unstructured grids, which has been used to accurately simulate a variety of marine flows including flow over hull (Kumar and Mahesh, 2018) and propellers (Verma et al., 2012; Jang and Mahesh, 2013; Jang et al., 2012; Kumar and Mahesh, 2017).

LES is performed for flow over the three-dimensional elliptical hydrofoil NACA 16-020, which has been used in numerous past studies (Fruman et al., 1995; Pichon et al., 1997; Boulon et al., 1999; Astolfi et al., 1999; Amini et al., 2019). Most LES of cavitation has been applied to attached or sheet-to-cloud regimes using compressible formulations of the homogeneous mixture equations. Inception occurs in the regime of low void fractions where the compressible governing equations can be argued to reduce to the zero-Mach equations which imply the use of the incompressible governing equations along with the same vapor volume fraction transport equation as the compressible equations (Brandao and Mahesh, 2022). Most numerical studies of tip vortex in the incipient regime employ a Euler–Lagrange framework, where the liquid follows the incompressible Navier–Stokes equations and each bubble is tracked individually with the equations of motion coupled with the Rayleigh–Plesset equation for their size (Hsiao et al., 2003; Hsiao and Chahine, 2005; Chen et al., 2019; Cheng et al., 2021). This approach can yield more details on the interactions of the nuclei and the tip vortex, at the extra cost of modeling the nuclei dynamics. Here, we use an extension to the model proposed by Brandao and Mahesh (2022) where vapor is treated as a passive scalar in a incompressible liquid. This extension assumes the vapor phase as a polydisperse distribution of bubbles divided discretely into bins of different sizes. Since the polydisperse is modeled as a passive scalar, the computational cost is considerably lower. The simulations are based on the experiments of Boulon et al. (1999). The goals of the present work are : (i) to demonstrate the capability of LES to simulate the complex flow field, and (ii) to study the tip vortex cavitation under different conditions.

The paper is organized as follows. The simulation details including the numerical method, hydrofoil geometry, computational grid and boundary conditions are described in Section 2, while a validation is provided in Section 3. The results are discussed in Section 4, and a summary in Section 5 concludes the paper.

2. Simulation details

2.1. Numerical method

In LES, large scales are directly accounted for by the spatially filtered Navier–Stokes equations, whereas the effect of small scales is modeled. The spatially filtered incompressible Navier–Stokes equations are as follows:

$$\frac{\partial \overline{u}_i}{\partial t} + \frac{\partial}{\partial x_j}(\overline{u}_i \overline{u}_j) = -\frac{\partial \overline{p}}{\partial x_i} + \nu \frac{\partial^2 \overline{u}_i}{\partial x_j \partial x_j} - \frac{\partial \tau_{ij}}{\partial x_j},$$
$$\frac{\partial \overline{u}_i}{\partial x_i} = 0, \tag{1}$$

where u_i is the velocity, p is the pressure divided by density, ν is the kinematic viscosity, the overbar $\overline{(.)}$ denotes the spatial filter and $\tau_{ij} = \overline{u_i u_j} - \overline{u}_i \overline{u}_j$ is the sub-grid stress. The dynamic Smagorinsky model proposed by Germano et al. (1991) and modified by Lilly (1992) is used to model the subgrid stress terms. The Lagrangian time scale is dynamically computed based on surrogate-correlation of the Germano-identity error (Park and Mahesh, 2009). This approach extended to unstructured grids has shown good performance for a variety of flows (Verma and Mahesh, 2012).

Eq. (1) is solved by a numerical method developed by Mahesh et al. (2004) for incompressible flows on unstructured grids. The algorithm is derived to be robust without any numerical dissipation. It is a finite volume method where the Cartesian velocities and pressure are stored at the centroids of the cells and the face normal velocities are stored independently at the centroids of the faces. A predictor–corrector approach is used. The predicted velocities at the control volume centroids are first obtained and then interpolated to obtain the face normal velocities. The predicted face normal velocity is projected so that the continuity equation in Eq. (1) is discretely satisfied. This yields a Poisson equation for pressure which is solved iteratively using a multigrid approach. The pressure field is used to update the Cartesian control volume velocities using a least-square formulation. Time advancement is performed using an implicit Crank–Nicholson scheme. The algorithm has been validated for a variety of problems over a range of Re as described in Section 1.

To account for the vapor phase, a cavitation model has to be included. Here we use an extension to the methodology presented in Brandao and Mahesh (2022) which was developed for the inception regime. In their work, a single transport equation for the vapor phase is computed, which accounts for the entire amount of vapor. Given that the amount of vapor produced in the inception regime is small, the changes in the mixture density is negligible. Thus, the vapor phase is treated as a passive scalar. The original unfiltered transport equation for the vapor phase, neglecting the diffusion term, is

$$\frac{\partial \rho_v \alpha}{\partial t} + \frac{\partial \rho_v \alpha u_j}{\partial x_j} = S, \tag{2}$$

where S is the cavitation source term. The vapor volume fraction is indicated by α and ρ_v is the vapor density, which is assumed constant.

The model has been validated against the results from a compressible homogeneous mixture model with a preconditioning methodology for the incipient regime in Brandao and Mahesh (2022). The extension we employ here assumes the vapor volume fraction is a polydisperse distribution of bubbles divided discretely into bins of different sizes at different concentrations per unit volume. This is visually exemplified in Fig. 1, where the bubbles radii are given by R and the bubble number density is given by N. Polydisperse models (also called population balance models) are less used to simulate cavitating flows when compared to more traditional models such as the homogeneous mixture model. More recently, however, a very comprehensive model was developed by Li and Carrica (2021) that includes bubble coalescence and breakup, and homogeneous and heterogeneous nucleation. The general form of the equation is given as

$$\frac{\partial f(m,\vec{x},t)}{\partial t} + \frac{\partial}{\partial x_j}\left(f(m,\vec{x},t)u_j\right) = RHS(m,\vec{x},t), \tag{3}$$

where $f(m,\vec{x},t)$ is the bubble size distribution function and represents the probable number of bubbles with mass in the range $(m, m+dm)$. The right-hand side of the equation accounts for breakage, coalescence and evaporation/condensation. Integrating Eq. (3) in the range $(m_{k-1/2}, m_{k+1/2})$ and ignoring the bubble coalescence and breakup terms, a transport equation for the bubble number density N_k for each group k is given as Li and Carrica (2021)

$$\frac{\partial N_k}{\partial t} + \frac{\partial N_k u_j}{\partial x_j} = \frac{\dot{m}_{k-1/2}}{m_k - m_{k-1}} N_{k-1/2} - \frac{\dot{m}_{k+1/2}}{m_{k+1} - m_k} N_{k+1/2}, \tag{4}$$

where $\dot{m}_{k\pm1/2}$ is the mass transfer term between adjacent bins, and $N_{k\pm1/2}$ is the bubble number density at the edge between bins, which here is taken as the average between N_k and $N_{k\pm1}$ although high order methods are recommended (Li and Carrica, 2021). The volume fraction of each bin can be written as $\alpha_k = N_k \frac{4\pi {R_k}^3}{3}$, where R_k is the radius of the bubbles in bin k, thus Eq. (4) can be rewritten as

$$\frac{\partial \rho_v \alpha_k}{\partial t} + \frac{\partial \rho_v \alpha_k u_j}{\partial x_j} = \frac{\dot{m}_{k-1/2}}{m_k - m_{k-1}} N_{k-1/2}\rho_v V_{bk} - \frac{\dot{m}_{k+1/2}}{m_{k+1} - m_k} N_{k+1/2}\rho_v V_{bk}. \tag{5}$$

Here, $V_{bk} = \frac{4\pi {R_k}^3}{3}$. The mass transfer term is based on the asymptotic solution of the Rayleigh–Plesset equation and is given by

$$\dot{m}_{k\pm1/2} = 4\pi\rho_v {R^2}_{k\pm1/2} sign(p_v - p)\sqrt{\frac{2}{3}\frac{|p_v - p|}{\rho_l}}, \tag{6}$$

where p_v is the vapor pressure and $R_{k\pm1/2}$ is the limiting radius between adjacent bins. It is evident from Eq. (5) that the amount of vapor in a bin is determined by the mass transfer between its adjacent bins and that the mass transfer between bins cancel each other out such that mass is conserved. Thus for the last bin, $\dot{m}_{k+1/2} = 0$. The vapor pressure is taken as a function of temperature as Saito et al. (2007)

$$p_v = p_k exp\left(\left(1 - \frac{T_k}{T}\right)(a + (b - cT)(T - d)^2)\right), \tag{7}$$

where $p_k = 22.130$ MPa, $T_k = 647.31$ K, $a = 7.21$, $b = 1.152 \times 10^{-5}$, $c = -4.787 \times 10^{-9}$ and $d = 483.16$. Brandao et al. (2020) show that this expression provides very good agreement with data from the National Institute of Standards and Technology (NIST). Given that we are interested in the inception regime, the vapor phase is treated as a passive scalar and Eq. (5) is solved following the numerical algorithm of Brandao and Mahesh (2022). A verification for this method is available in Appendix.

2.2. Hydrofoil geometry, computational grid and boundary conditions

The problem setup closely resembles the reference experiments of Boulon et al. (1999). The hydrofoil has a NACA 16-020 cross-section and an elliptical planform of span $S = 0.18$ m, a root chord length

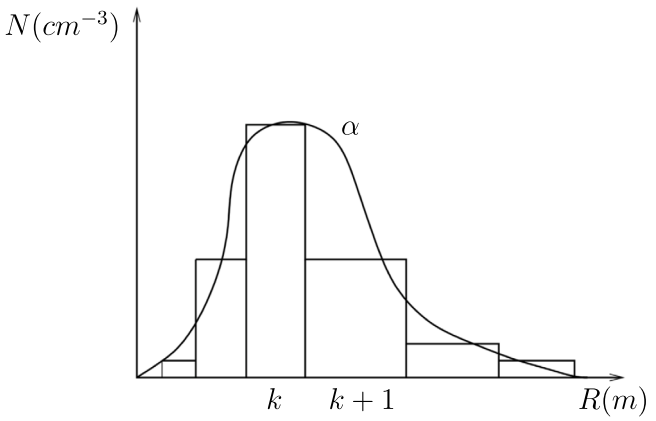

Fig. 1. Example of a distribution of bubbles of different sizes.

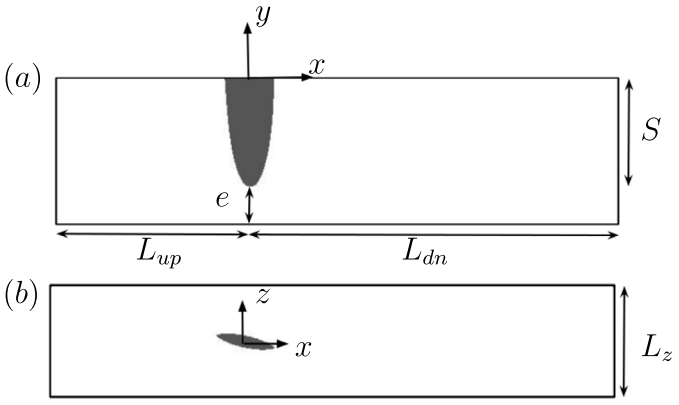

Fig. 2. Schematic of the computational domain shown in $z = 0$ (a) and $y = 0.1$ (b) planes.

$c = 0.12$ m and the aspect ratio is 3.8. The hydrofoil is mounted such that the mid point of the root chord of the hydrofoil is the origin of the Cartesian coordinate system and the tip is located at $(0, -S, 0)$. The hydrofoil span aligns with the y axis and x is the downstream streamwise direction. The two side walls are located at $z = \pm L_z/2$, where $L_z = 0.175$. Note that one grid unit is equivalent to 1 m length in the reference experiment. Hence, the tip-gap $e = 0.06$ which corresponds to the experimental setup of $e = 60$ mm, is generally chosen as the reference case corresponding to no confinement due to the bottom wall. As stated in the reference paper, the two side walls cause confinement resulting in a 27% increase of lift. The Re based on c and U_∞ are 9×10^5 and 1.4×10^6, and the hydrofoil is rotated about y to make an angle of attack of 12 degrees. The inflow and outflow planes are located at $L_{up} = 2.58c$ upstream and $L_{dn} = 4.92c$ downstream of the tip respectively. The schematic of the computational domain is shown in Fig. 2.

Freestream velocity is prescribed at the inflow and convective boundary conditions are applied at the outflow. All other domain boundaries have no-slip boundary conditions. A coarse grid (not shown here) of 14 million hexahedral control volumes is first used to assess grid resolution and obtain a solution which is used to initialize a fine grid simulation containing 44 million hexahedral control volumes, which is nominally two times finer in each direction compared to the coarse grid in the near field everywhere except near wall (no-slip) boundaries. The span of the hydrofoil has more than 260 cells and there are more than 400 cells in z direction for the fine grid. The gap between tip of the hydrofoil and the bottom wall contains more than 80 cells. The tip vortex is resolved over more than 20 cells, which is in line with

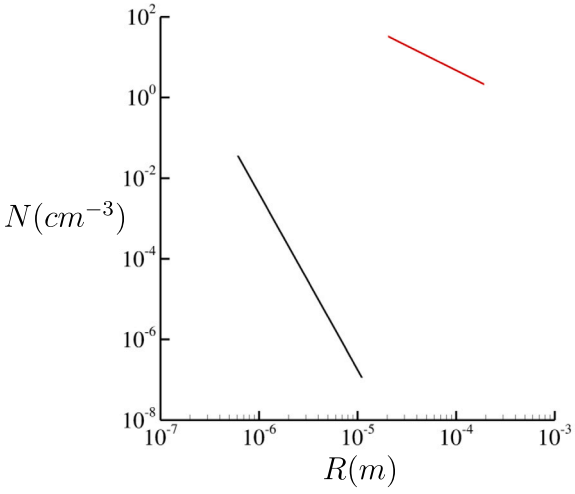

Fig. 3. Bubble distribution at inflow for natural (black) and seeded cases (red). (For interpretation of the references to color in this figure legend, the reader is referred to the web version of this article.)

the simulations of hydrofoil tip vortex by Asnaghi et al. (2017, 2020). The grid is clustered near all the wall boundaries with a nominal wall-normal first cell size of $8.3\times10^{-4}c$ and $1.67\times10^{-3}c$ at hydrofoil surface and other walls respectively with a growth rate of one percent. All the results presented in this paper are normalized appropriately using U_∞ and c, except when the units are explicitly mentioned. The flow is taken to be at room temperature, which yields $p_v \approx 2$ kPa.

We assume that the bubble distribution ranges from 0.5 μm to 5 mm and it is divided into 8 bins. The amount of vapor prescribed at the inflow follows the conditions from the water tunnel at the Australian Maritime College investigated in the work of Khoo et al. (2020c). Two distributions are studied, named as "natural" and "seeded", corresponding to conditions where the water is poor and rich in nuclei respectively. They are shown in Fig. 3. It is important to mention that the water can also be called as "strong" or "weak", depending whether the flow is poor or rich in nuclei, respectively. Those distributions yield an overall inflow vapor void fraction of $\alpha \approx 6.1\times10^{-15}$ and 1.85×10^{-4} for the natural and seeded cases respectively. The cavitation number is chosen to be $\sigma = 2.1$, which is the critical value reported by Boulon et al. (1999) for the angle of attack and confinement value used in the present work. It is important to mention that the critical cavitation number is defined in Boulon et al. (1999) as the value at which the vapor core attaches to the tip. Thus, the critical σ is lower than the inception σ, which is the value at which the first instance of cavitation is observed.

3. Comparison to experiments

Before comparing the results with the experimental data, a discussion on the experimental setup is necessary. Boulon et al. (1999) performed the reference experiments. They could vary Re from 3.6×10^5 to 1.4×10^6 in their hydrodynamic tunnel by varying U_∞ from 3 to 12 m/s. Their tunnel had a freestream turbulence of 1.5% with empty test section. Most of their experiments were conducted at $U_\infty = 7$ m/s, which corresponds to $Re = 9\times10^5$. For example, they showed images (their Fig. 4) visualizing tip vortex cavitation at different tip gaps at the same U_∞ and an angle of attack $\alpha = 12°$. Hence, $\alpha = 12°$ was chosen as the angle of attack for the simulations. However, the measurements of the velocity profiles in the wake at a range of tip gaps were only reported at the same α but a lower $U_\infty = 5$ m/s. Assuming the other quantities remained unchanged, this U_∞ in the tunnel would make $Re \approx 6.4\times10^5$ for the experiments where the profile measurements were taken.

The strength of the tip vortex depends on the overall lift generated by the hydrofoil whereas its core size correlates with the boundary layer thickness (McCormick, 1962). Billet and Holl (1981) showed that for a variety of wing shapes and cross sections at Re greater than that corresponding to flat plate boundary layer laminar–turbulent transition ($Re \approx 5\times10^5$), the minimum pressure coefficient $C_{p,min}$ on the axis of the tip vortex (modeled as a Rankine vortex) scales as

$$C_{p,min} = kC_l^2 Re^{0.4}, \tag{8}$$

where k is a constant which depends on the foil and C_l is the lift coefficient. The present hydrofoil, however, deviates from this behavior. Fruman et al. (1995) showed that, for same C_l and $Re = 1.2\times10^6$, the behavior of elliptic foils deviates from straight leading and trailing edge foils, in that the elliptic foil cavitates earlier. They later showed that this behavior is not related to Re, but can be associated with water quality. Moreover, $C_{p,min}$ drops further below at lower Re due to a large change in C_l. This peculiar behavior of the present hydrofoil makes it different than other hydrofoils and wings.

Pichon et al. (1997) studied the effect of tripping the boundary layer over the present hydrofoil on the tip vortex behavior and showed that the tip vortex in the tripped boundary layer case at $Re < 5.6\times10^5$ not only behaved like that generated by untripped hydrofoil at higher Re but also followed Eq. (8). This behavior suggests complex dependence of the tip vortex on the hydrofoil boundary layer which depends on both Re and α. Note that the transition $Re = 5.6\times10^5$ was for unconfined tip vortex. The presence of side and bottom walls can alter the transition Re by modifying the hydrofoil boundary layer on either sides, thereby making the overall flow field highly sensitive to Re close to the transition value. Note that Boulon et al. (1999) did not trip the hydrofoil boundary layer and the reported profiles were measured at Re close to the transition Re. Due to these reasons, it is suspected that the hydrofoil boundary layer in the reference experiments were not

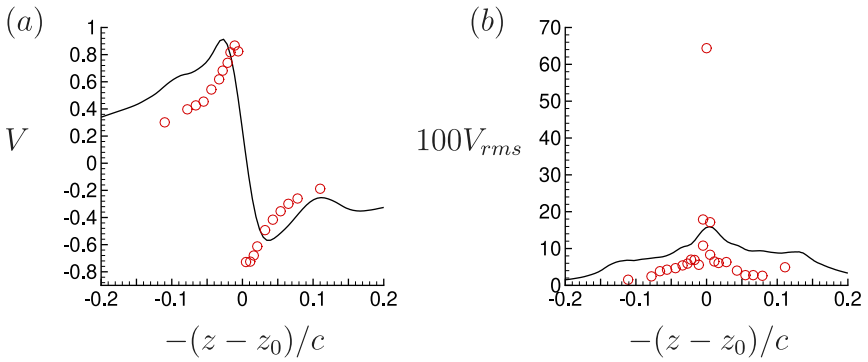

Fig. 4. The LES results are compared to the experiments (Boulon et al., 1999) for mean (V) (a) and r.m.s. (V_{rms}) (b) of vertical velocity at $x/c = 1$. Note that z_0 is the location of the tip vortex core on the horizontal line passing through it.

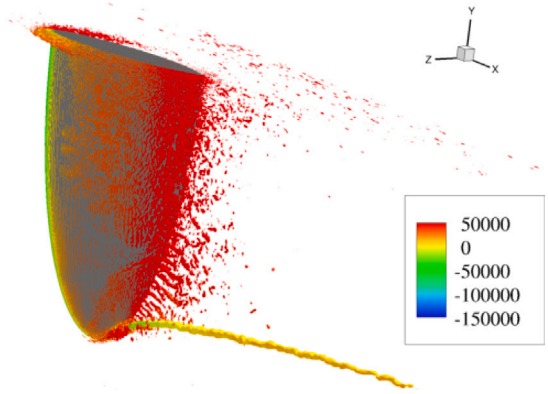

Fig. 5. Isocontour of λ_2 colored with pressure in Pa showing the trailing edge wake and the tip vortex. The bottom and side walls are removed for visualization.

turbulent. In fact, we will see in Section 4 that bulk of the flow on the hydrofoil appears laminar.

The results are compared to the mean profiles of mean and root-mean-square (r.m.s) of vertical velocity at $x/c = 1$ available from the experiments in Fig. 4. Note that the results are plotted similar to that in the experiment. The results show reasonable agreement with the experiment. No other profile measurements were reported at these conditions.

4. Results

4.1. Overview of the flow field

The results presented in this section are obtained at $Re = 9 \times 10^5$. The instantaneous coherent vortical structures in the flow field are visualized using the isocontour of λ_2 (Jeong and Hussain, 1995) colored with pressure as shown in Fig. 5. Note that the bottom and side walls are removed for clear visualization. The incoming flow accelerates on the pressure side and decelerates on the suction side of the hydrofoil. The pressure difference across the hydrofoil creates lift. The variation of local lift along the span causes vortex shedding at the trailing edge of the hydrofoil, forming a vortex sheet which terminates into a coherent tip vortex. The tip vortex can be seen as a coherent vortex originating near tip on the suction side, whose axis is aligned with the freestream (x) direction. The tip vortex appears coherent throughout the simulated domain.

The instantaneous pressure, axial velocity and vorticity magnitude in $z = 0$ plane are shown in Fig. 6. The tip vortex is visible clearly as the region of low pressure and high vorticity. The pressure minimum at a given downstream location occurs in the tip vortex core and its magnitude decreases moving downstream. The streamwise velocity field shows shear layers in the wake, with a small region of flow separation near the trailing edge. Fig. 6(c) shows that there are three main regions of high vorticity: the tip vortex, the trailing edge and the boundary layers on the no-slip boundaries. In order to have a closer look at the flow, a slice is extracted $y/c = -0.83$ and shown in Fig. 7. The flow appears attached everywhere except very close to trailing edge. The vorticity shed from the trailing edge forms a shear layer, which evolves downstream under the influence of side-walls. The velocity defect and vorticity magnitude in the wake decays moving downstream.

The instantaneous pressure and vorticity fields in the wake are shown at $x/c = 1$ in Fig. 8. The pressure variation from the ambient can be observed in the trailing vortex sheet and the tip vortex, with the tip vortex being the local pressure minimum. The overall wake appears as a line vortex terminating into a tip vortex, which undergoes the process of spiral roll-up in counterclockwise sense in the figure shown. The boundary layers can be observed on all wall boundaries. The streamwise, vertical and horizontal components of instantaneous velocity are shown in Fig. 9. The velocity jumps across the shear layer are visible. Note the existence of high streamwise velocity near the axis of symmetry, which distinguishes the trailing edge vortices from other types of line vortices (Batchelor, 1964).

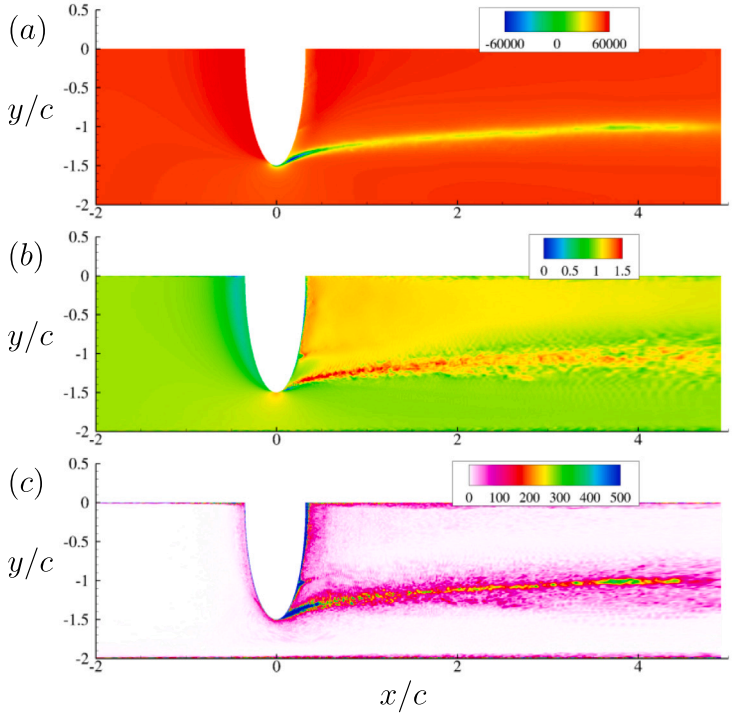

Fig. 6. Instantaneous flow field showing pressure in Pa (a), streamwise velocity (b) and vorticity magnitude (c) in $z = 0$ plane.

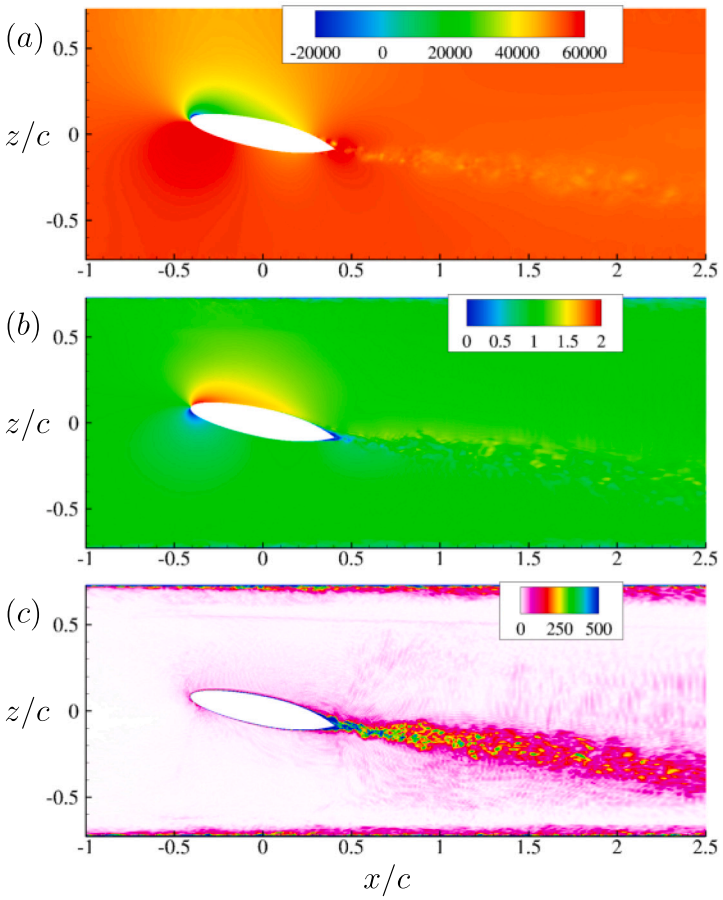

Fig. 7. Instantaneous flow field showing pressure in Pa (a), streamwise velocity (b) and vorticity magnitude (c) in $y/c = -0.83$ plane.

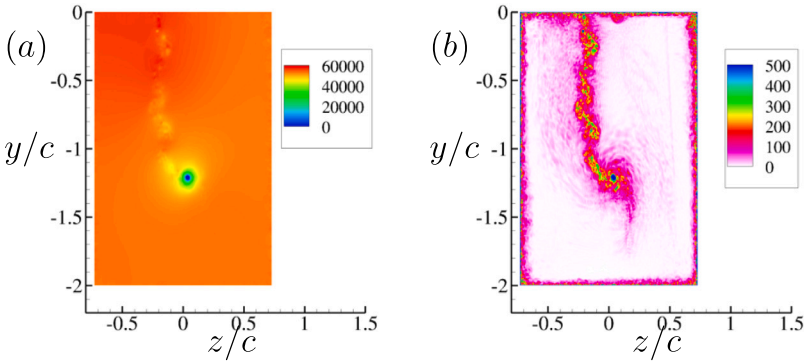

Fig. 8. Instantaneous flow field showing pressure in Pa (a) and vorticity magnitude (b) at $x/c = 1$.

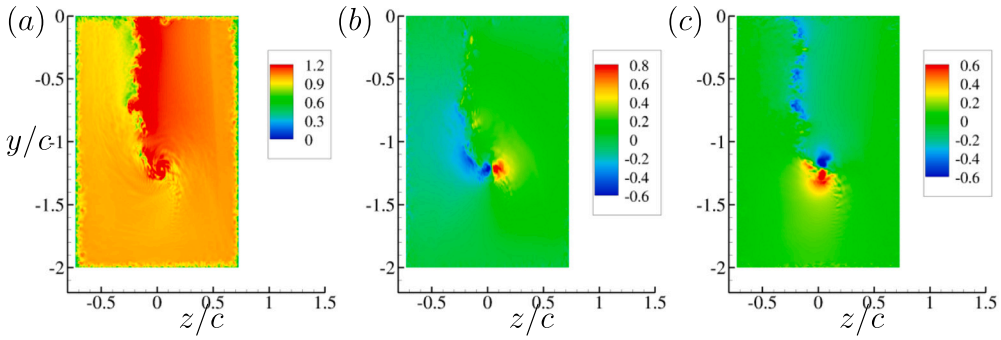

Fig. 9. Instantaneous velocity components in streamwise (a), vertical (b) and horizontal (c) directions at $x/c = 1$.

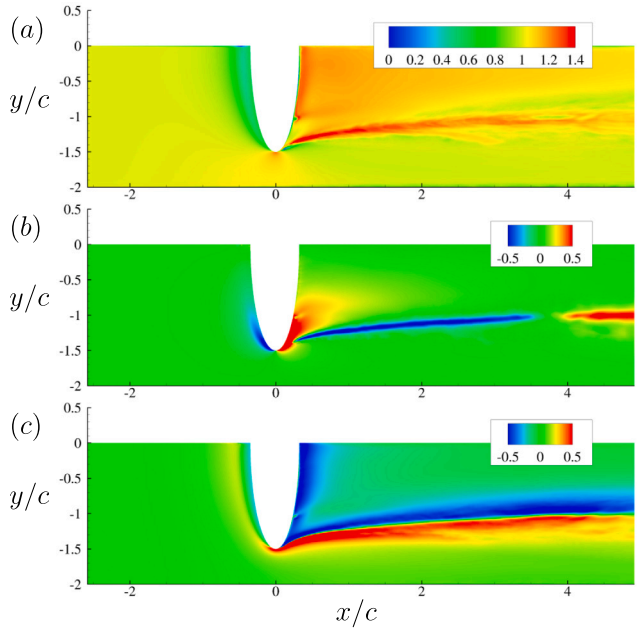

Fig. 10. Mean velocity components in axial (a), vertical (b) and horizontal (c) directions are shown in $z = 0$ plane.

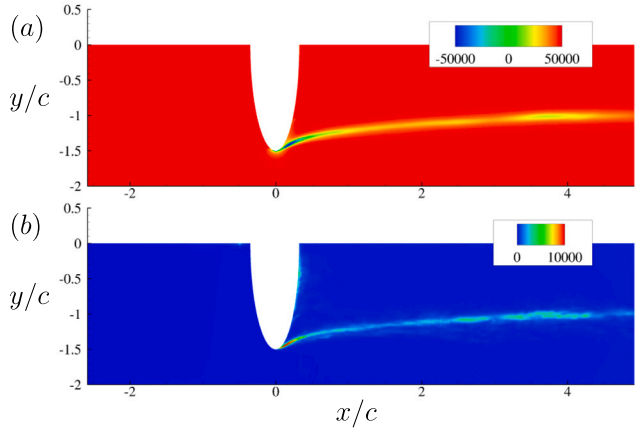

Fig. 11. Mean (a) and rms (b) values of pressure in Pa.

Fig. 10 shows the mean velocity components in $z = 0$ plane. The shear layer appears to grow in the y direction in all the components moving downstream. The region in the vicinity of the tip has large magnitude of vertical velocity mainly due to the end effects where the flow tends to move from the pressure side to the suction side. The horizontal component of mean velocity shows the mean swirl of the axial tip vortex. The mean and root-mean-square values of pressure are given in Fig. 11. The mean minimum value of pressure is found to be in the vortex core very close to the hydrofoil tip, which is a region of high water tension (negative pressure). In addition, the entire tip vortex experiences very high levels of pressure fluctuation, which makes it susceptible for inception. Fig. 12 shows components of turbulent intensity at $x/c = 1$. The axial component dominates the wall boundary layers whereas all the components are of same order for the wake. The boundary layer of the bottom wall is far away from the tip vortex core.

4.2. Cavitation characteristics

Prior to a presenting the results it is important to discuss the criteria used to identify inception. Inception is usually identified by visual or acoustic techniques. Visually, inception is detected when cavitating structures larger than a certain size are observed. However, there is no consensus about the threshold. Agarwal et al. (2018) in a experimental study of inception at turbulent shear layers, identified inception when a bubble grows larger than 157 μm. In numerical simulations using the Euler–Lagrange framework, Bappy et al. (2022) assumed that inception had occurred when a bubble became larger than 500 μm, while Park et al. (2009) used the threshold of 1 mm. When the vapor phase is modeled in a Eulerian framework, the volume fraction is commonly employed as the variable that identifies inception. Cheng et al. (2021), e.g., visualized incipient structures by iso-surfaces of $\alpha = 0.1$. Here, we assume inception occurs when the volume fraction of the last bin, which contains bubbles larger than 1 mm, is greater than 0.001.

4.2.1. Effects of water quality

The results presented in this subsection are obtained at $Re = 9\times10^5$. A comparison between cases at $Re = 9 \times 10^5$ and $Re = 1.4 \times 10^6$ is given in Section 4.2.3. Fig. 13 displays the iso-surfaces of $\alpha = 0.001$ for bubbles larger and smaller than 1 mm for the natural and seeded cases at a instant of time. We can observe some features from both cases. First, we can see that the maximum total void fraction for both cases is very small ($O(-3)$). Taking the mixture density as the volumetric average between the phases densities, $\rho = \alpha\rho_v + (1-\alpha)\rho_l$, this maximum void fraction would yield a total change in the mixture density of less than 0.1% if a homogeneous mixture approach was used, confirming that it is the incipient regime and that treating the vapor phase as a passive scalar is appropriate. The cavitation topology is very different between each case. In the natural case, inception is found to be an intermittent event confined to the tip vortex at a position close to the hydrofoil's tip. The region undergoing inception is so tiny that it is hard to visualize it in Fig. 13(a), therefore a zoomed view is provided in Fig. 14. In addition, the concentration of bubbles smaller than 1 mm does not amount to $\alpha = 0.001$. In the seeded case (Fig. 13(b)), cavitation at the tip vortex is fully developed, showing a protuberant structure connected to the hydrofoil's tip. This behavior is consistent with the visual observations from Boulon et al. (1999) at the critical cavitation number. These differences between each case are consistent

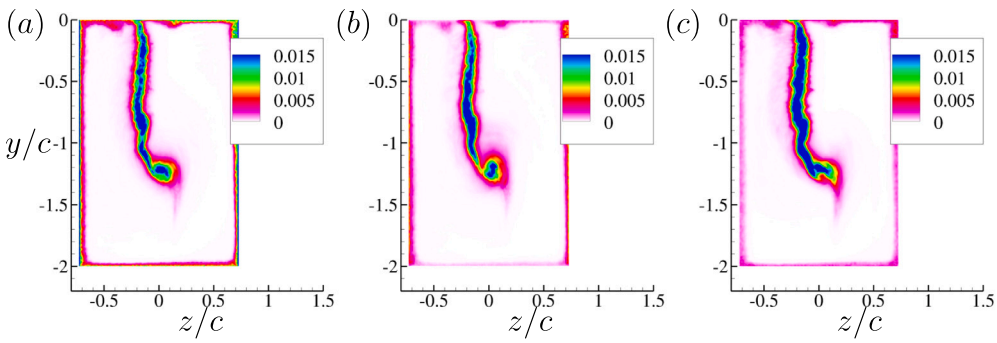

Fig. 12. Turbulent intensities in streamwise (a), vertical (b) and horizontal (c) directions are shown at $x/c = 1$.

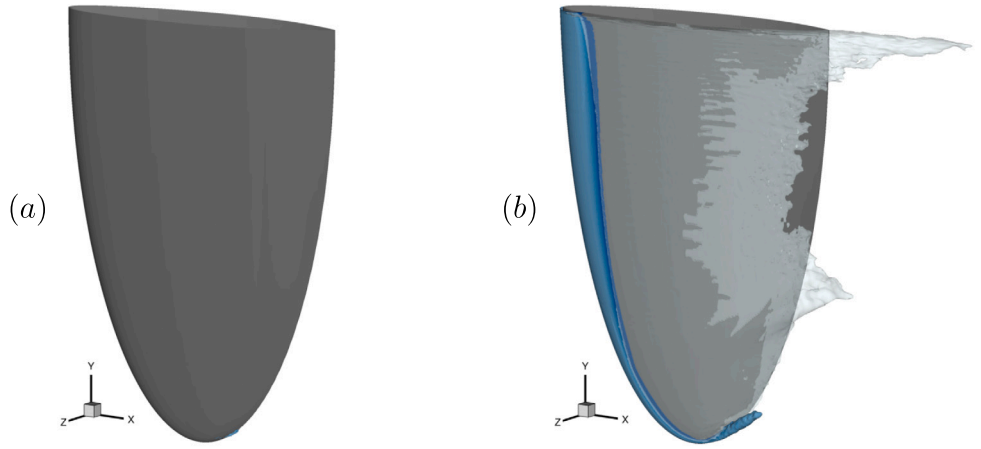

Fig. 13. Iso-surfaces of $\alpha = 0.001$ for bubbles larger (blue) and smaller (transparent light gray) than 1 mm for the natural (a) and seeded (b) cases. (For interpretation of the references to color in this figure legend, the reader is referred to the web version of this article.)

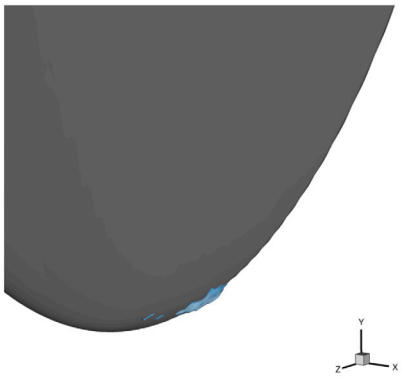

Fig. 14. Zoomed view of an iso-surfaces of $\alpha = 0.001$ for bubbles larger than 1 mm for the natural case.

with experimental observations (Arndt and Maines, 2000) and highlight that the inception cavitation number for the seeded case is much higher than for the natural case. The seeded case also provide some unique features. Given the continuous supply of large nuclei in the freestream, part of the suction side very close to the leading edge of the hydrofoil also experience cavitation. Furthermore, the entire suction side is covered with a layer of bubbles smaller than 1 mm.

The probability density functions (PDF) of $\alpha \geq 0.001$ for bubbles larger than 1 mm for both cases are given in Fig. 15(a) (indicating regions of cavitation), while the PDFs of a region experiencing a pressure lower than vapor pressure and experiencing the minimum pressure of the entire domain is displayed in Fig. 15(b). We can observe that the likelihood of cavitation is well aligned with the likelihood of a region experiencing values of pressure lower than the vapor pressure for the seeded case. For the natural case however, inception only happens in the regions most likely to experience extreme low values of pressure. In addition, for the natural case, inception is confined to a region around $x/c = 0.1$, which is within the range observed in the literature for strong water (Arndt and Maines, 2000; Khoo et al., 2020a). The maximum value of the concentration per unit volume for bubbles larger than 1 mm in each case is presented in Fig. 16(a) and (b). The corresponding power spectra densities (PSD) showing the dominant frequencies are given in Figs. 16(c) and (d). It can be observed that the flow experiences a highly intermittent and chaotic explosive growth in number of bubbles for the natural case. This behavior is a direct consequence of the extreme and random pressure fluctuations of flows with high Re. When the flow is rich in nuclei, this behavior becomes less chaotic and a dominant frequency for the explosive increase in bubbles is visible. Here it is important to remind that our model is one-way coupled, meaning that the amount of vapor in each case is not affecting the pressure field. Thus, this result indicates that inception in a flow rich in nuclei is less affected by the pressure fluctuations than in a flow depleted in nuclei.

The PDF of the total volume of vapor produced (for bubbles larger than 1 mm) is given in Fig. 17 for both natural and seeded cases.

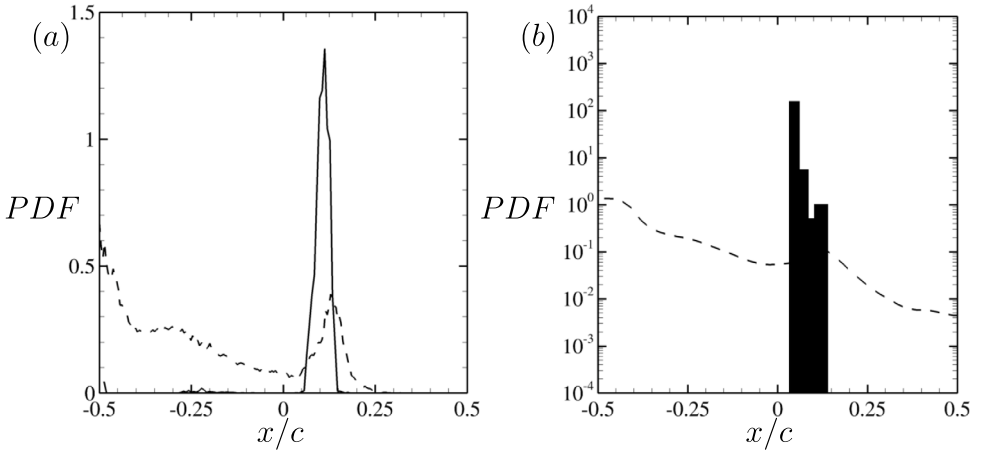

Fig. 15. PDFs of $\alpha \geq 0.001$ for bubbles larger than 1 mm are given in (a) for the natural (solid line) and seeded (dashed line). PDFs of $p < p_v$ (dashed line) and minimum pressure (bar) are given in (b).

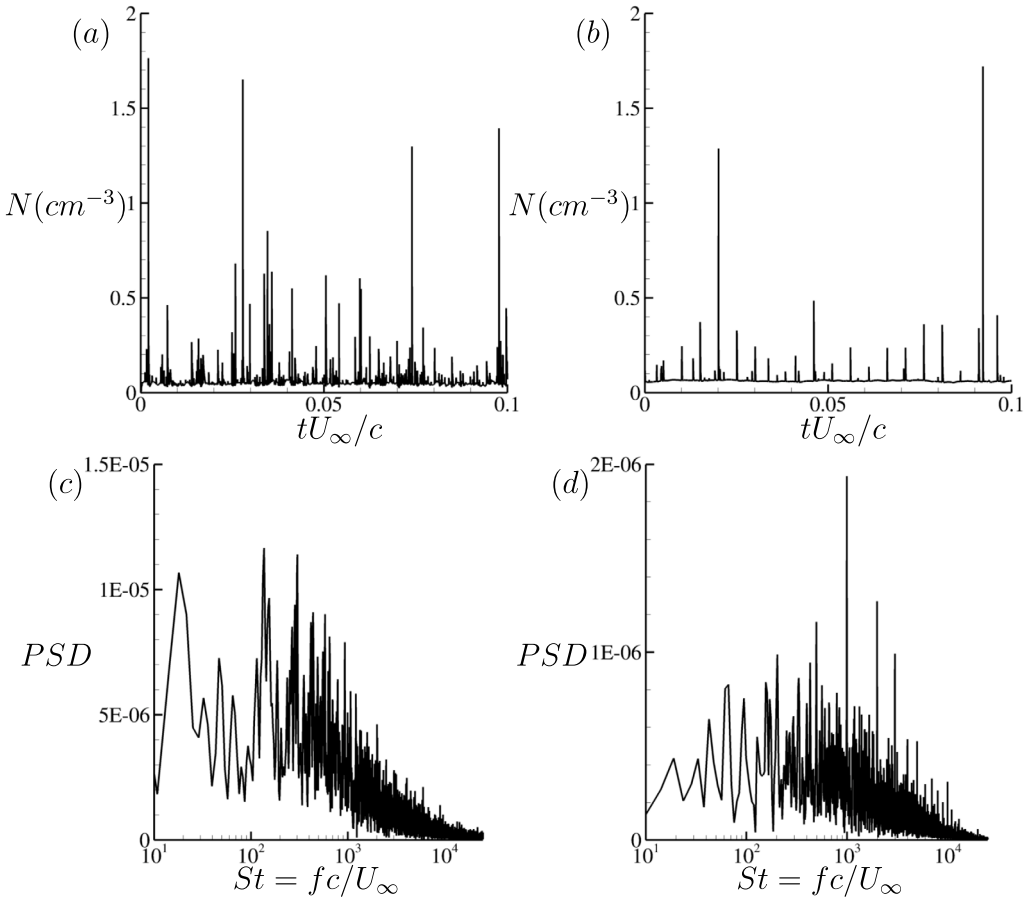

Fig. 16. Time history of maximum concentration per unit volume for bubbles larger than 1 mm for the natural (*a*) and seeded (*b*) cases at $Re = 9 \times 10^5$. Power spectra density of the signals are also given for the natural (*c*) and seeded (*d*) cases.

The seeded case produces a volume of vapor around $O(2)$ larger than the natural case, which is expected. The range of values of volume produced in the natural case is, however, much broader. The difference between the minimum and maximum values is $O(1)$. The amount of vapor produced in the seeded case is almost "fixed" changing very little in time, forming a stable cavity as seen in Fig. 13. This also confirms the trend observed in Fig. 16(*a*) and (*b*).

The vapor volume fraction for some bubble bins (0.5 μm - 1 μm, 5 μm - 10 μm and 1 mm - 5 mm) are displayed in Fig. 18 and show their evolution across the wake. We can observe that the amount of void fraction for the small bubble groups (0.5 μm - 1 μm and 5 μm - 10 μm) very close to the hydrofoil is larger for the seeded case than it is for the natural one, despite these groups not being present at the inflow for the former. Furthermore, the evolution of these group along the wake differs considerably between each case. At close distances from the hydrofoil, these small bubbles are concentrated in the trailing vortex sheet for both cases. However for the natural case, this behavior persists beyond $x/c = 4$, while for the seeded case they are homogeneously distributed across the section area already at $x/c = 3$. This happens because the condensation process is proportional to the bubble number density (see Eq. (5)), which is proportional to the void fraction. Thus the larger values of volume fractions closes to the hydrofoil yields faster condensation rates as pressure is recovered downstream of the hydrofoil. Figs. 19(*a*) and (*b*) show mean bubbles distributions at the hydrofoil tip ($x/c = 0$, $y/c = -1.5$) and at the center of the tip vortex ($x/c = 0.225$, $y/c = -1.4$) for both natural and seeded cases. At the foil tip, the concentration of bubbles for the seeded case are in general orders of magnitude larger than for the natural case, although they

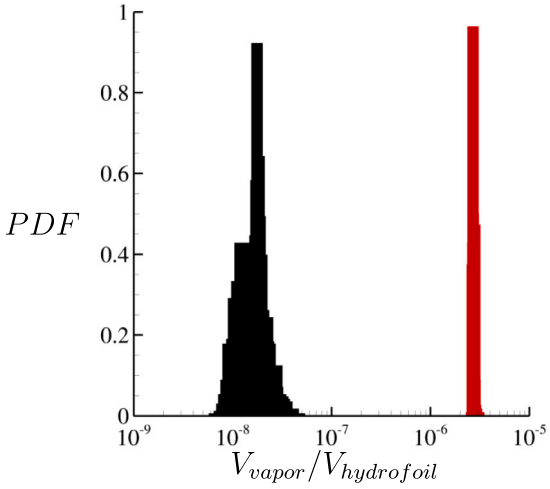

Fig. 17. Volume of vapor produced in the natural (black) and seeded case (red) scaled with the volume of the hydrofoil. (For interpretation of the references to color in this figure legend, the reader is referred to the web version of this article.)

quickly become comparable at the tip vortex. In addition, a contrasting behavior can be observed after the flow travels from the foil tip to the tip vortex. The overall concentration of bubbles of different sizes increases when the flow is poor in nuclei, but drop when it is rich in nuclei, consistent with the predictions from Fig. 18.

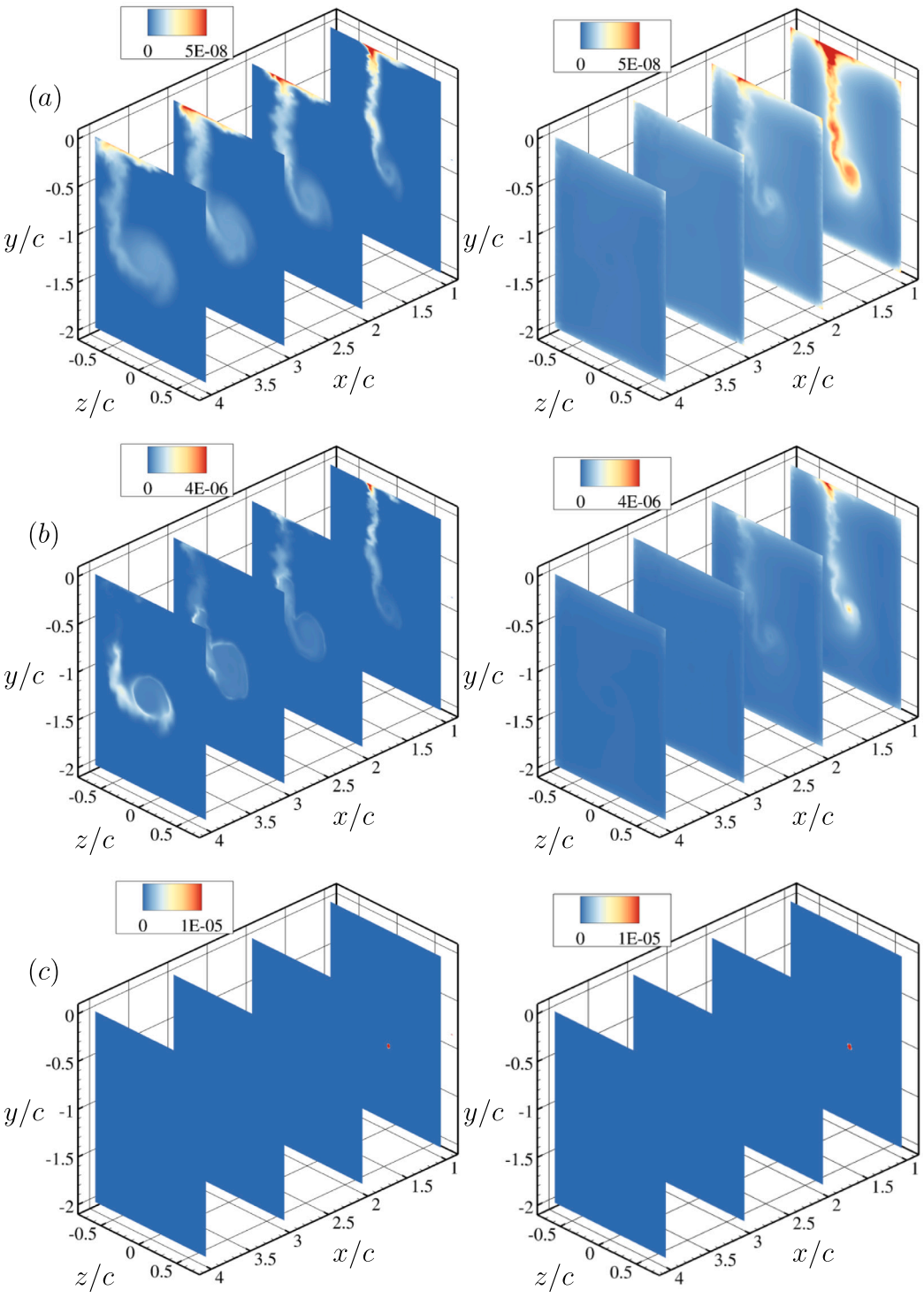

Fig. 18. Vapor volume fraction of different bubble bins: 0.5 μm - 1 μm (*a*), 5 μm - 10 μm (*b*) and 1 mm - 5 mm (*c*) for the natural (left) and seeded (right) cases at $Re = 9 \times 10^5$.

4.2.2. Flow topology

In this work, we examine the incipient structures by studying their flow topology based on the invariants of the velocity gradient tensor, strain rate tensor and rotation rate tensor. Chong et al. (1990), Cantwell (1992) and Perry and Chong (1994) discuss the details of this approach; only a summary of the invariants and their physical meaning will be given here. The velocity gradient tensor, $A_{ij} = \frac{\partial u_i}{\partial x_j}$, has the following characteristic equation:

$$\lambda_i^3 + P\lambda_i^2 + Q\lambda_i + R = 0, \tag{9}$$

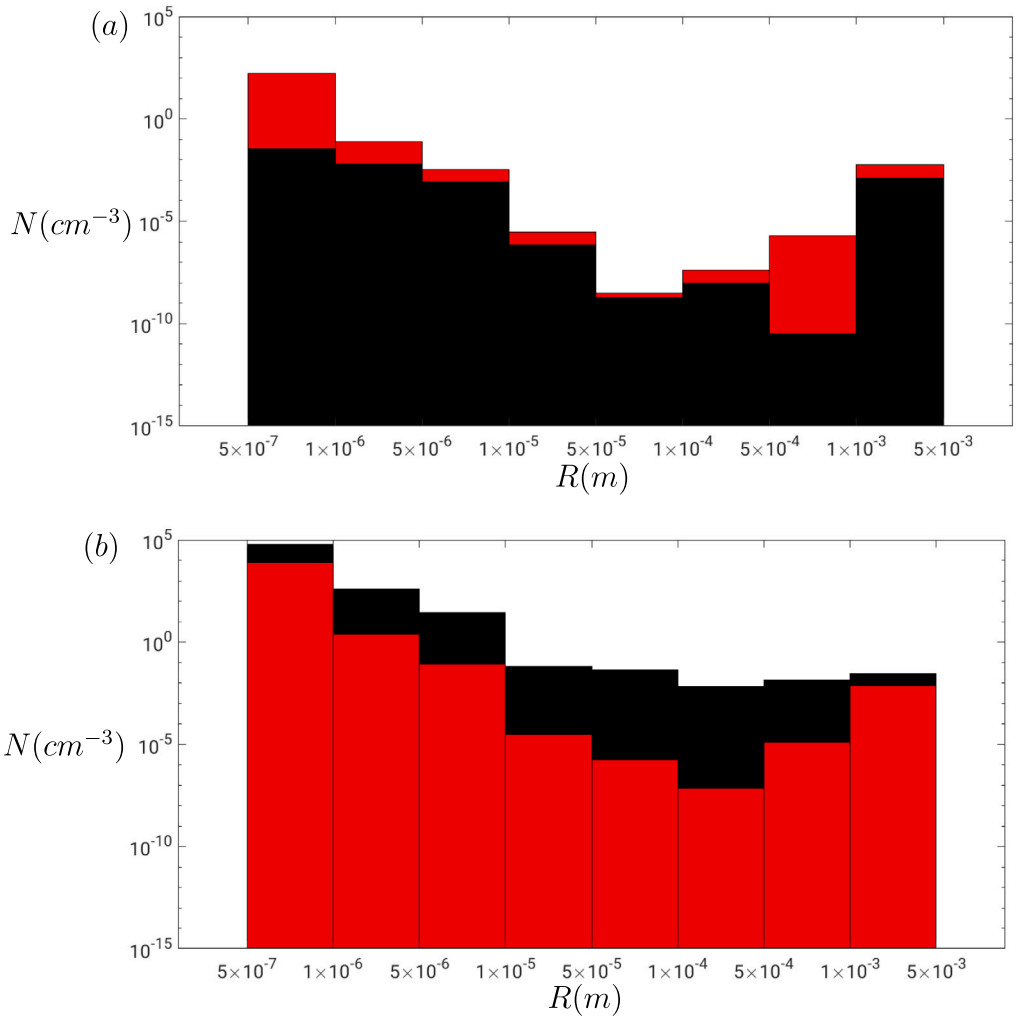

Fig. 19. Mean bubble distribution at the hydrofoil tip (black) and at tip vortex (red) for the natural (*a*) and seeded (*b*) cases at $Re = 9\times10^5$. (For interpretation of the references to color in this figure legend, the reader is referred to the web version of this article.)

where λ_i are the eigenvalues and P, Q and R are the first, second and third invariants of A_{ij}, respectively. These invariants are given by

$$\begin{aligned} P &= -S_{ii}, \\ Q &= \frac{1}{2}(P^2 - S_{ij}S_{ji} - \Omega_{ij}\Omega_{ji}), \\ R &= \frac{1}{3}(-P^3 + 3PQ - S_{ij}S_{jk}S_{ki} - 3\Omega_{ij}\Omega_{jk}S_{ki}). \end{aligned} \tag{10}$$

Here, $S_{ij} = \frac{A_{ij}+A_{ji}}{2}$ and $\Omega_{ij} = \frac{A_{ij}-A_{ji}}{2}$ are the strain rate tensor and rotation rate tensor, respectively. $P = 0$ due to incompressibility. Likewise, the invariants of S_{ij} and Ω_{ij} are defined by their respective characteristic equation. For incompressible flows, only the second and third invariants of S_{ij} and the second invariant of Ω_{ij} are non-zero. They are given by the following expressions:

$$Q_s = -\frac{1}{2}S_{ij}S_{ji}, \quad R_s = -\frac{1}{3}S_{ij}S_{jk}S_{ki} \quad \text{and} \quad Q_w = -\frac{1}{2}\Omega_{ij}\Omega_{ji}, \tag{11}$$

where the subscripts S and w indicate that the variable is related to the strain rate tensor and rotation rate tensor, respectively.

Fig. 20(a) shows the topologies in the Q–R plane. The tent-like curve depicts $D = 0$, where D is the discriminant of A_{ij} given by $D = \frac{27}{4}R^2 + Q^3$. Fluid elements occupying the region of $D > 0$ are focal regions and can be undergoing stretching ($R < 0$) or contraction ($R > 0$). According to Ooi et al. (1999), the focal structures with stretching topology are in general elongated and compact in a tube-like shape, while the contracting regions resemble 'blobs' and are usually found at the ends of the focal structure or at the intersection between two stretching regions. Fig. 20(b) shows the physical interpretation for the Q_s–Q_w plane. Regions of the flow lying below the $Q_w = -Q_s$ line are dominated by rotation (such as the core of a vortex tube) while regions lying above the line are dominated by strain (such as the periphery of a vortex tube) with intense kinetic energy dissipation. The flow topology has been investigated in numerous problems. da Silva and Pereira (2008) studied the invariants in a turbulent/nonturbulent interface by using a direct numerical simulation of a turbulent plane jet, and found out that the flow points are characterized by irrotational dissipation at the interface. More recently, Brandao and Mahesh (2022) studied the topologies of incipient structures in a shear layer. Their results revealed that inception is more likely to occur in the cores of stretched vortices. The invariants of the regions where and when $\alpha \geq 0.001$ for bubbles larger than 1 mm are computed, and their joint-PDF are given in Fig. 21 showing the topology of the incipient structures for the natural case.

The joint-PDF of Q–R in Fig. 21(*a*) shows that inception more likely occurs in the stretched focal regions. The joint-PDF of Q_s–Q_w in Fig. 21(*b*) reveals that regions dominated by irrotational strain are favorable places of inception. In other words, the periphery of stretched vortices have higher likelihood of inception. The ratio between rotational strength and irrotational straining rate of a flow element is given by the kinematical vorticity number (Truesdell, 1954), and is defined

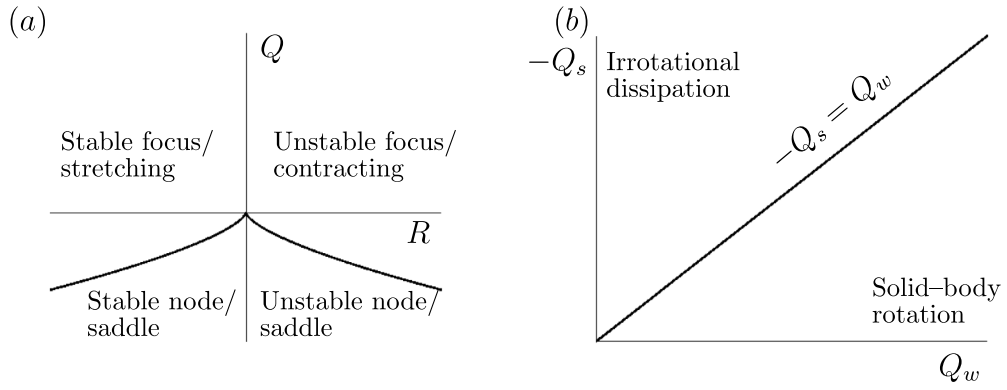

Fig. 20. The regions formed by the second and third invariants of the velocity gradient tensor (Q–R) and the regions formed by the second invariants of the strain rate tensor and rotation rate tensor (Q_s–Q_w) are given in (a) and (b) respectively with their corresponding flow patterns.

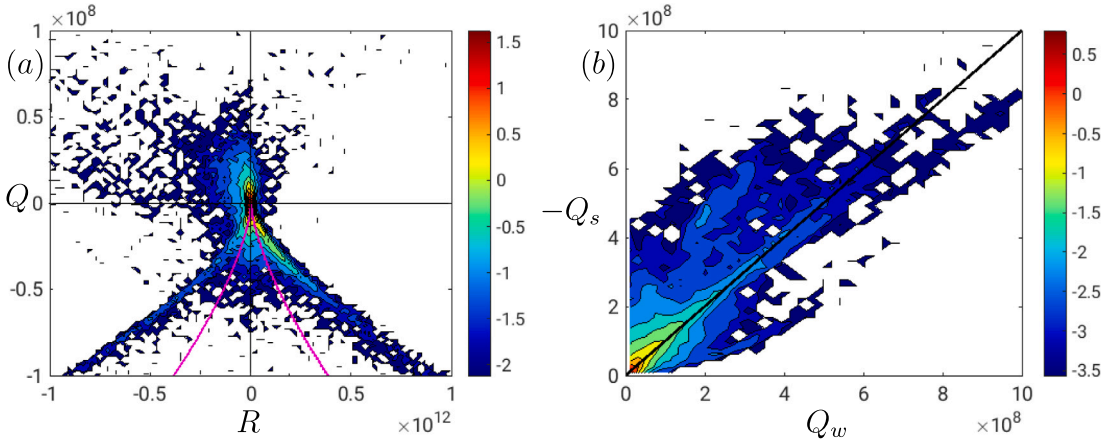

Fig. 21. Joint-PDFs of Q–R (a) and Q_s–Q_w (b) of the incipient regions for the natural case. Levels in both plots are in logarithmic scale and the invariants are in non-dimensional units (using the appropriate combination of the root chord length, c, and the freestream velocity, U_∞). The pink tent-like curve represents the discriminant of the velocity gradient tensor. (For interpretation of the references to color in this figure legend, the reader is referred to the web version of this article.)

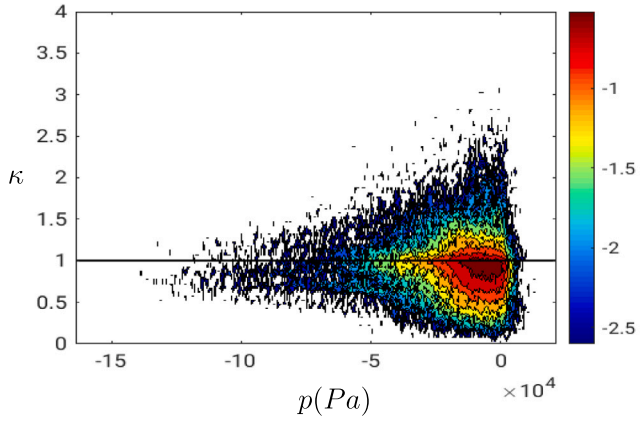

Fig. 22. Joint-PDF between pressure and κ. The line of $\kappa = 1$ signals the boundary between stretching to rotation dominated.

as

$$\kappa = \left(\frac{Q_w}{-Q_s}\right)^{\frac{1}{2}}. \tag{12}$$

A value of $\kappa = 0$ implies that a fluid particle is undergoing purely irrotational stretching while a value of $\kappa = \infty$ means that the fluid particle is subjected only to solid-body rotation. The joint-PDF between pressure and κ is displayed in Fig. 22 and reveals a predominance of $\kappa \approx 0.75$, which means that inception is most likely to occur when the vortex has a stretching rate around 1.8× larger than its rotation rate. The results from Figs. 21 and 22 are in contrast with those obtained for inception in a shear layer by Brandao and Mahesh (2022), where inception was found to occur primarily in regions dominated by rotation. We believe that these differences are mainly due to the differences in the flow configuration between both works, as well as the difference in the threshold used for inception detection. Brandao and Mahesh (2022) use $p < p_v$, instead of bubbles size, as a criteria for inception. It can also be observed that, although inception occurs primarily when the stretching rate dominates, a wide range of κ can lead to inception at vapor pressure, including values that indicate that the flow is dominated by rotation. However, this range narrows down as pressure drops. The lowest values of pressure leading to inception occurs exclusively when that flow region is dominated by stretching. Another quantity of interest is defined by Ooi et al. (1999) as

$$\Sigma = \frac{R_s - R}{Q_w}, \tag{13}$$

that represents the rate at which the vorticity is stretched ($\Sigma > 0$) or contracted ($\Sigma < 0$). Fig. 23 shows the joint-PDF between κ and Σ of the incipient structures. The plot reveals a preference for positive straining rate (indicating vorticity stretching), consistent with Fig. 21(a). Interestingly, the plot also reveals that the larger vorticity stretching rates of the inception structures are associated with $\kappa \approx 1$. Fig. 24(a), (b) and (c) displays isocontours of λ_2, showing the tip vortex surrounded

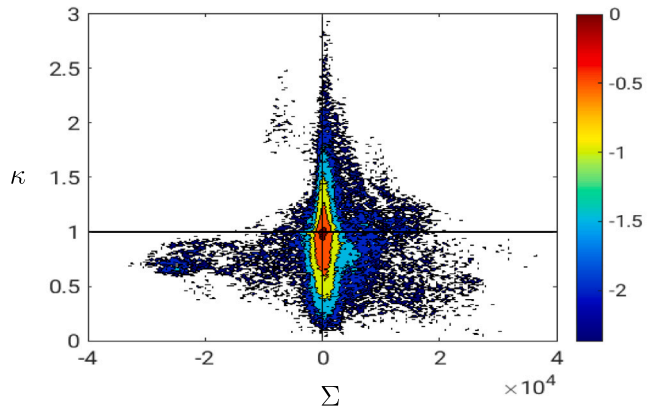

Fig. 23. Joint-PDF between Σ and κ. Levels are in logarithmic scale and the black line indicates $\kappa = 1$.

by smaller secondary vortices, colored by α, κ and Σ respectively. We can see that vapor is found in the initial part of the tip vortex, surrounded by the smaller secondary vortices, and that this is a region dominated by the irrotational straining with high stretching rates. As the tip vortex moves further downstream and ceases to be surrounded by the secondary vortices, it starts to become dominated by rotation ($\kappa > 1$) and presents larger contraction rates ($\Sigma < 0$).

4.2.3. Effects of Reynolds number

Inception was also investigated at a higher Reynolds number ($Re = 1.4 \times 10^6$ with $U_\infty = 12$ m/s) at the same cavitation number ($\sigma = 2.1$). The time history of the maximum concentration per unit volume of bubbles larger than 1 mm and the PSD of its respective signal are given in Fig. 25 for the natural and seeded cases. Differently from the conditions at $Re = 9 \times 10^5$, both cases experience a chaotic pattern of growth in number of large bubbles without any clear dominant frequency. The probability density function of $\alpha \geq 0.001$ for bubbles larger than 1 mm at the two values of Re is displayed in Fig. 26 for the natural case. Although the two values of Re are relatively close to each other, it can be seen that the inception location moves slightly downstream with increasing Re. Fig. 27(*a*) and (*b*) shows the PDF of total volume of vapor produced (for bubbles larger than 1 mm) for the natural and seeded cases, respectively. It can be seen that increasing Re but keeping σ the same, in this case, does not significantly change the volumes of vapor produced, although there is a modest increase for the seeded case. It becomes evident when comparing Fig. 17 with Fig. 27, that water quality has a much larger effect on the amounts of vapor produced than the Re, for the incipient regime. It can also be concluded that if the flow is depleted of nuclei, the Reynolds number has little effect on the inception behavior. The joint-PDFs between Q–R, Q_s–Q_w, pressure and κ, and κ–Σ of the incipient structures are given in Figs. 28(*a*) and (*b*), and Figs. 29(*a*) and (*b*), respectively, for the natural case. It is evident that they show the same behaviors as those observed for the $Re = 9 \times 10^5$ case.

The effect of Re on inception is explained here by tracking particles injected from the hydrofoil tip and investigating their pressure history at both Re, in an effort to emulate the pressure history that vapor nuclei would experience. These particles are assumed to follow the liquid velocity, hence their positions are obtained as

$$\frac{d\vec{x}}{dt} = \vec{u}. \tag{14}$$

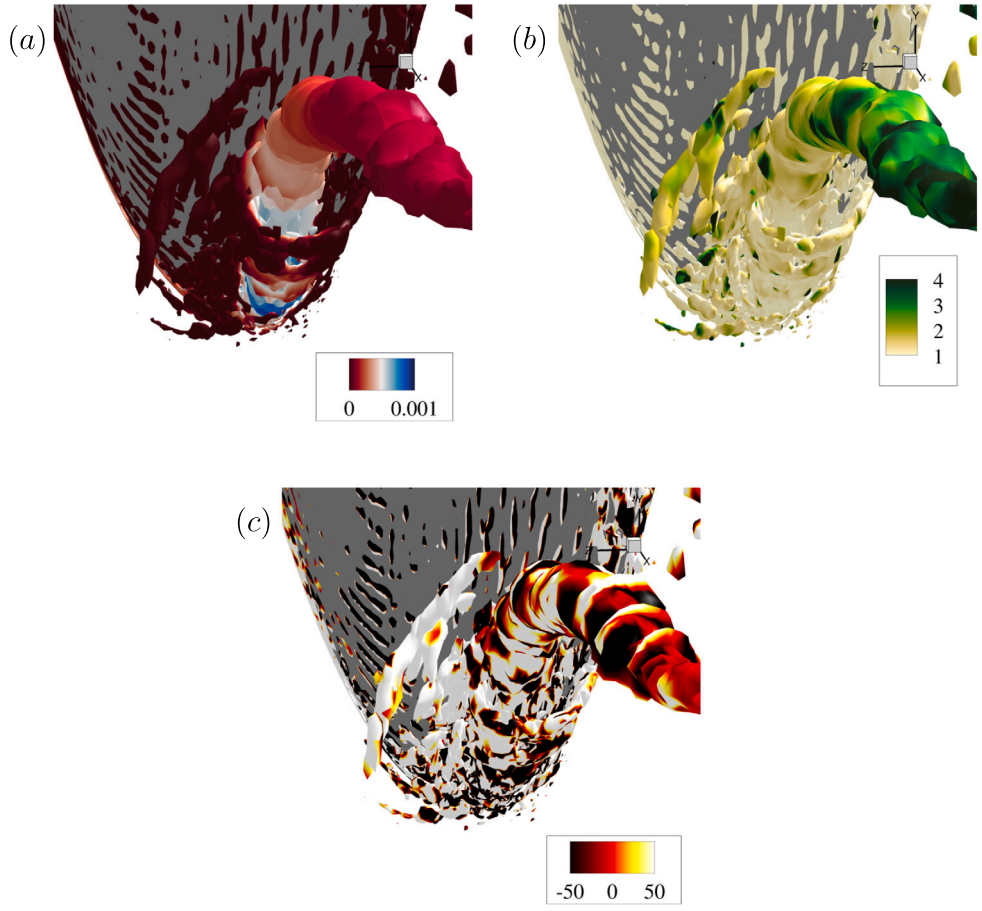

Fig. 24. Frontal view of the tip vortex and secondary vortices colored with the vapor volume fraction (*a*), κ (*b*) and Σ (*c*).

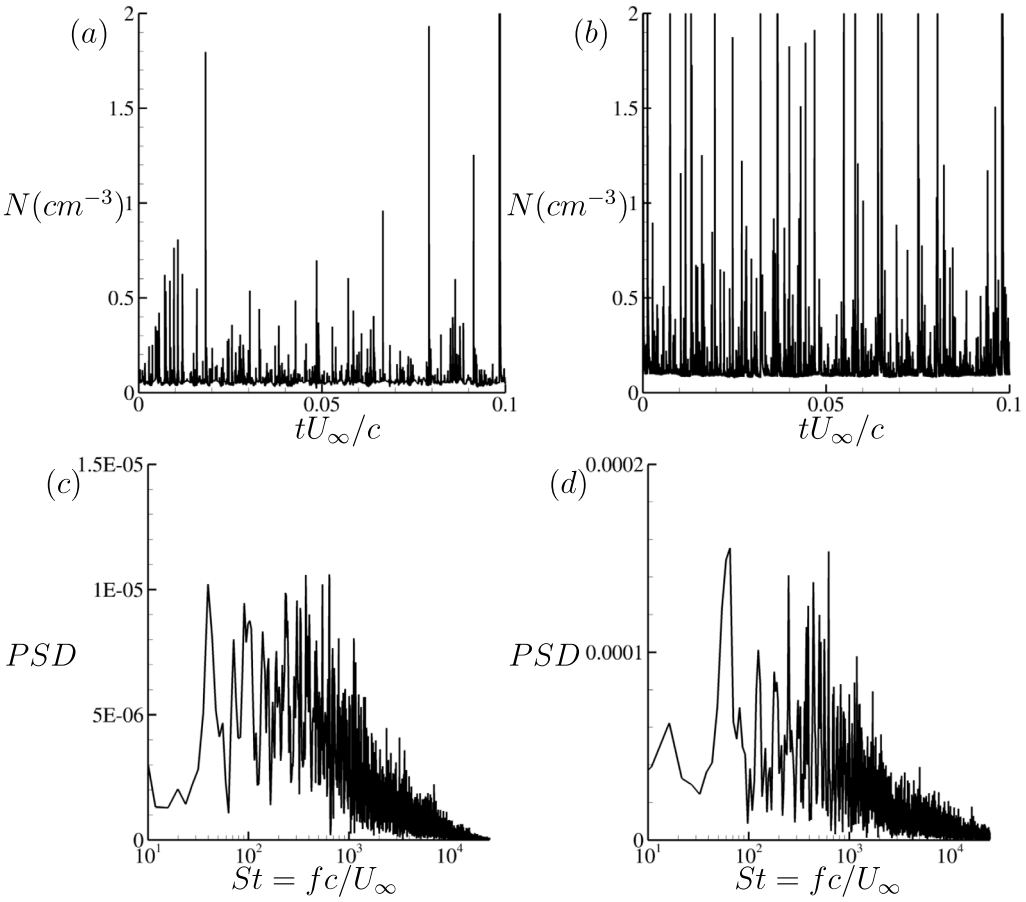

Fig. 25. Time history of maximum concentration per unit volume for bubbles larger than 1 mm for the natural (*a*) and seeded (*b*) cases at $Re = 1.4 \times 10^6$. Power spectra density of the signals are also given for the natural (*c*) and seeded (*d*) cases.

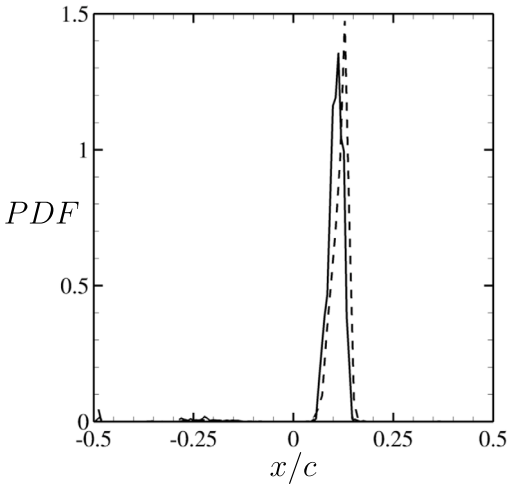

Fig. 26. PDFs of $\alpha \geq 0.001$ for bubbles larger than 1 mm for $Re = 9 \times 10^5$ (solid) and $Re = 1.4 \times 10^6$ (dashed).

We inject 1000 particles from the hydrofoil tip for both *Re* studied in Section 4.2.3. Fig. 30 shows example of the particles trajectories and the pressure history that some of them experience. From Fig. 30(*a*), we can see that the particles move in a spiral course following the tip vortex direction.

The PDFs for the Lagrangian pressure histories of the particles at both *Re* are presented in Fig. 31. As expected, higher *Re* yields a broader spectrum of pressure values. It is important to remind that both *Re* cases were simulated at the same inflow cavitation number of 2.1, which means that the inflow pressure at $Re = 1.4 \times 10^6$ is much larger than at $Re = 9 \times 10^5$. Despite that, the plot shows that even if increasing *Re* is accompanied by an increase in ambient pressure, the particles still have a higher likelihood of experiencing extreme low values of pressure. It also shows that the particles have a much larger likelihood of experiencing higher values of pressure with increasing *Re*. Fig. 32 shows the cumulative distribution functions of the total time that the particles experience pressure lower than vapor pressure. It can be seen that the probability of a particles spending shorter periods of time at a pressure lower than vapor pressure increases with increasing *Re*. This reinforces and help to explain the trend observed in Fig. 27 where *Re* did not have an impact on the amounts of vapor produced. The reason behind this is that inception requires that the low pressure acting on small vapor structures to be sustained for some time. Therefore, the volume of vapor produced at inception with an increase in *Re* at the same σ is mostly unchanged.

5. Summary

LES is performed to investigate cavitation inception over an elliptical hydrofoil at two different values of *Re* and at $\sigma = 2.1$. The numerical model presented in Brandao and Mahesh (2022) is extended to include multiple groups of bubbles of different sizes. This modification allows for the investigation of the effects of water quality on inception. We study two different conditions: one when the flow is poor in nuclei (called "natural" distribution) and the other when the flow is rich in nuclei (called "seeded" distribution). It was found that inception characteristics change drastically depending on the water quality. When

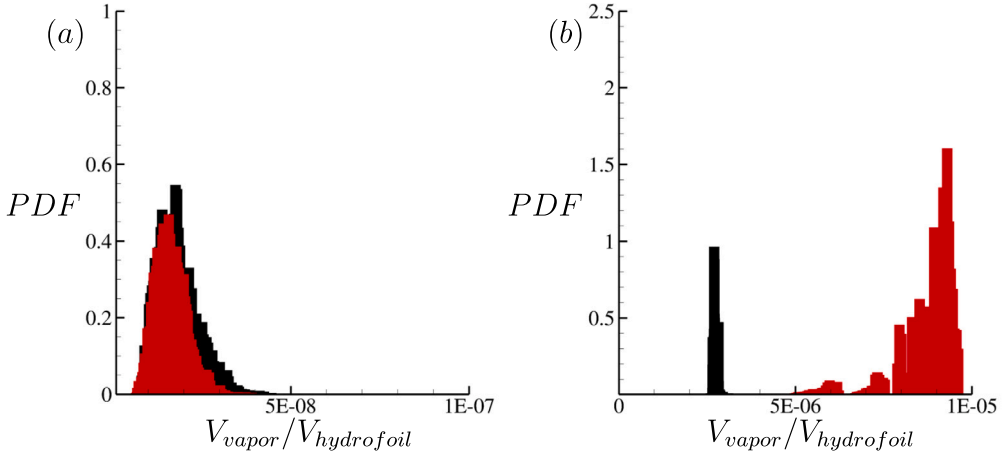

Fig. 27. Volume of vapor produced in the natural (*a*) and seeded (*b*) cases at $Re = 9\times10^5$ (black) and $Re = 1.4\times10^6$ (red) scaled with the volume of the hydrofoil. (For interpretation of the references to color in this figure legend, the reader is referred to the web version of this article.)

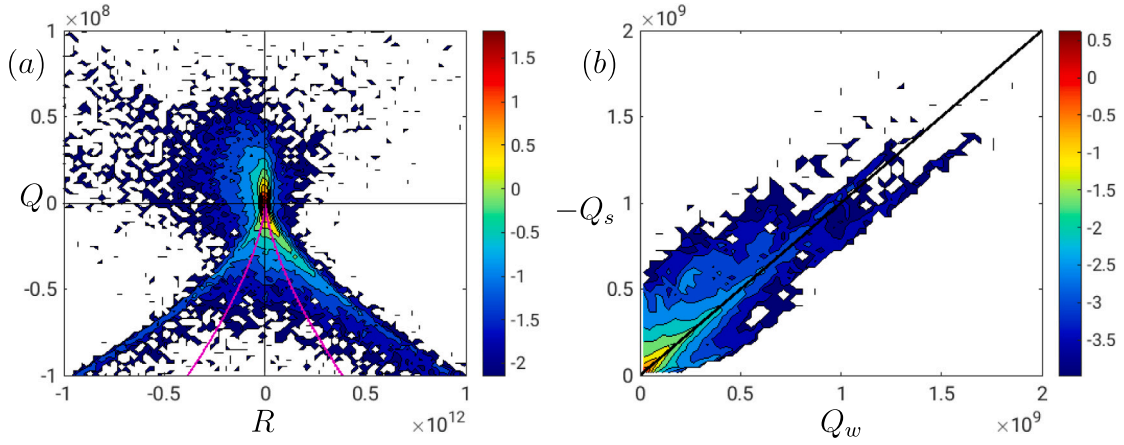

Fig. 28. Joint-PDFs of Q–R (*a*) and Q_s–Q_w (*b*) of the incipient regions for the natural case at $Re = 1.4\times10^6$. Levels in both plots are in logarithmic scale and the invariants are in non-dimensional units (using the appropriate combination of the root chord length, c, and the freestream velocity, U_∞). The pink tent-like curve represents the discriminant of the velocity gradient tensor. (For interpretation of the references to color in this figure legend, the reader is referred to the web version of this article.)

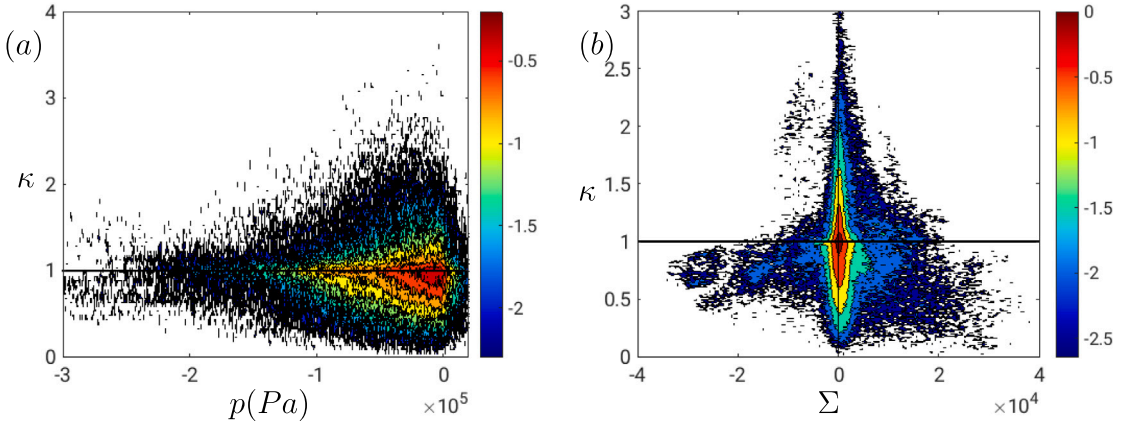

Fig. 29. Joint-PDF between pressure and κ (*a*) and between Σ and κ (*b*) for $Re = 1.4\times10^6$. Levels are in logarithmic scale and the black line indicates $\kappa = 1$.

the flow is depleted of nuclei, inception was found to occur in the regions with extremely low values of pressure (usually kPa of tension). In contrast, when the flow is rich in nuclei, inception occurs anywhere that experience pressure lower than vapor pressure. The volume of vapor produced for the seeded case is orders of magnitude larger than for the natural case, with vapor being formed along the tip vortex and on the leading edge of the foil. This is in contrast with the natural case where vapor formation is an intermittent event confined to a small region close to the foil's tip. The results showed that the explosive growth in number of bubbles at $Re = 9\times10^5$ is chaotic for the natural case, with no dominant frequency. For the seeded case, however, this behavior becomes less chaotic and a dominant frequency appears. With

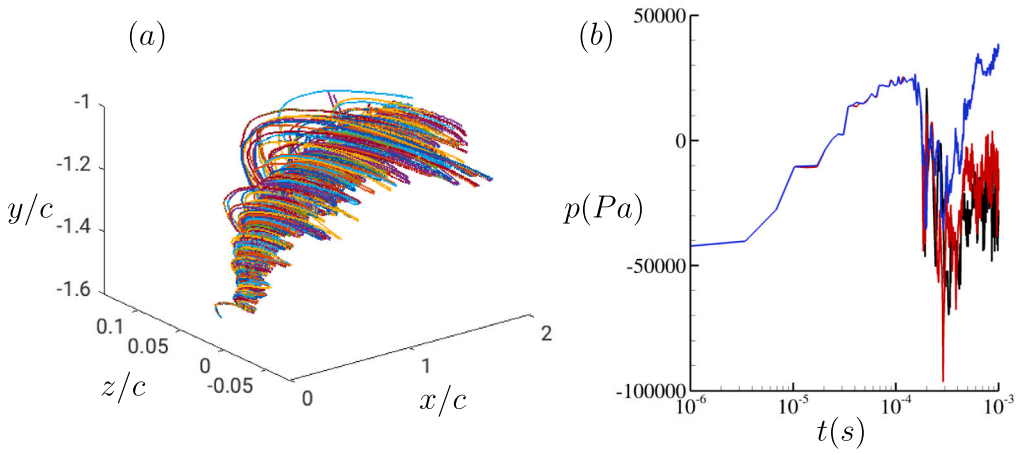

Fig. 30. Particles trajectories are given in (*a*), where each line corresponds to the path of one of the 1000 particles. Pressure history of only three particles are given in (*b*) for better visualization. Both plots are obtained for $Re = 9 \times 10^5$.

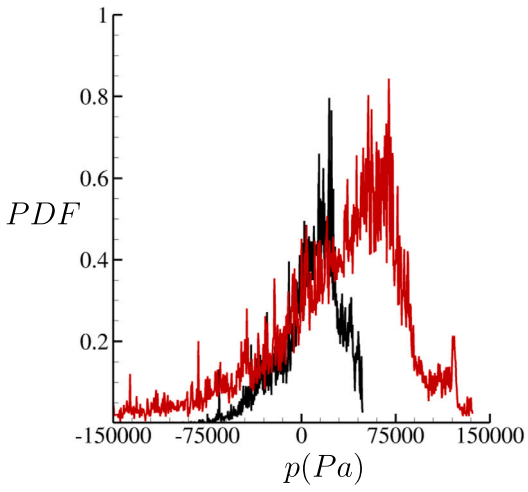

Fig. 31. PDFs of lagrangian pressure history for the 1000 particles injected at $Re = 9 \times 10^5$ (black) and $Re = 1.4 \times 10^6$ (red). (For interpretation of the references to color in this figure legend, the reader is referred to the web version of this article.)

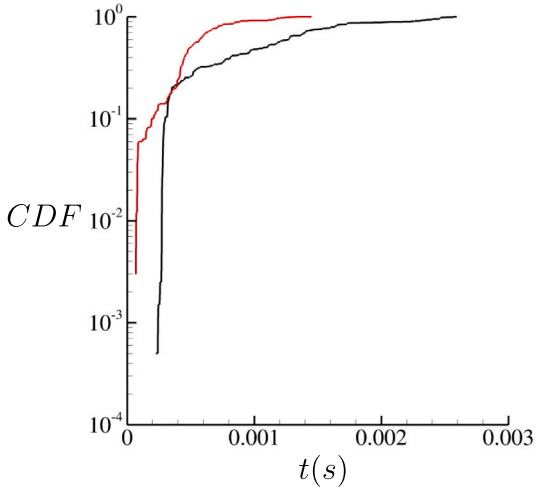

Fig. 32. CDFs of the total time bubbles experience pressure lower than vapor pressure at $Re = 9 \times 10^5$ (black) and $Re = 1.4 \times 10^6$ (red). (For interpretation of the references to color in this figure legend, the reader is referred to the web version of this article.)

an increase in *Re*, both flow conditions experience a chaotic growth of number of bubbles. It was found that water quality has a bigger impact on inception than the *Re*, and that inception characteristics are mostly unaffected by the change in *Re* when the flow is very depleted of nuclei. The inception location remains unchanged with increasing *Re* when the flow is poor in nuclei. In addition, the increase in the volume of vapor produced with increasing *Re* was found to be less than $O(1)$ for the seeded case and negligible for the natural case. To help explain that, particles were released from the foil's tip and tracked in an effort to emulate the pressure history that vapor structures would be subjected to. The results indicated that, although vapor structures would have higher likelihood of experiencing very low values of pressure with increasing *Re*, the amount of time they are under these low values of pressure is reduced. The flow topology of the incipient structures were investigated for the natural case, and it was found that inception have a higher likelihood to occur in focal regions dominated by irrotational straining with high stretching rates.

CRediT authorship contribution statement

Filipe L. Brandao: Data curation, Formal analysis, Investigation, Methodology, Writing – original draft, Writing – review & editing. **Praveen Kumar:** Data curation, Formal analysis, Investigation, Writing – original draft, Writing – review & editing. **Krishnan Mahesh:** Conceptualization, Funding acquisition, Methodology, Supervision, Writing – original draft, Writing – review & editing.

Declaration of competing interest

The authors declare that they have no known competing financial interests or personal relationships that could have appeared to influence the work reported in this paper.

Data availability

Data will be made available on request.

Acknowledgments

This work is supported by the United States Office of Naval Research under grant ONR N00014-17-1-2676 with Dr. Ki-Han Kim and Dr. Yin-Lu Young as the program managers. Computing resources were provided by the High-Performance Computing Modernization Program (HPCMP).

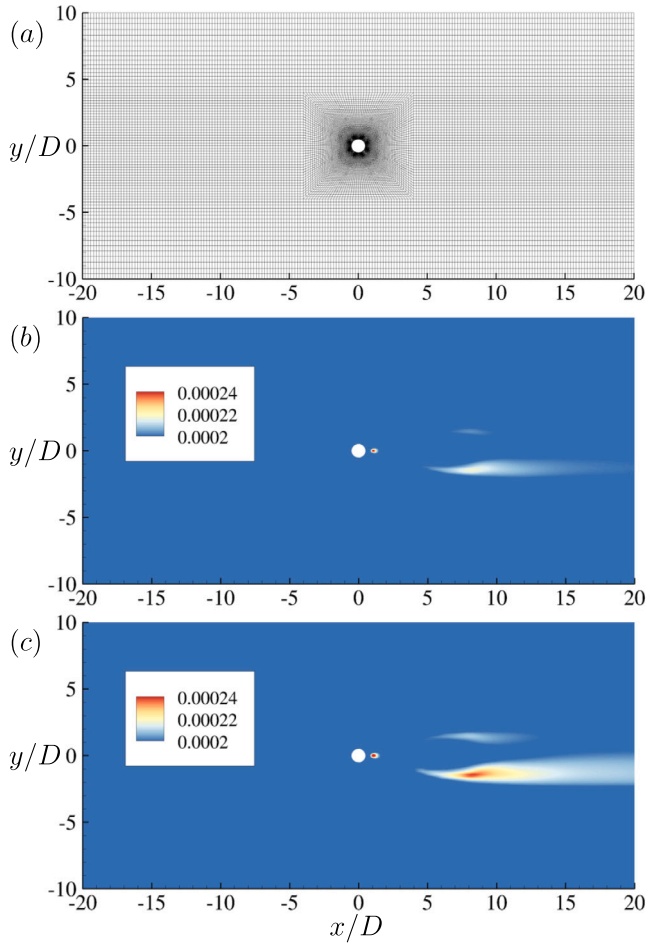

Fig. A.33. Computational domains (*a*). Mean values of total vapor volume fraction when the polydisperse model is employed (*b*) and when it is not (*c*).

Appendix. Verification of the method

The method described in this work is a extension of the work presented in Brandao and Mahesh (2022) where vapor is treated as a passive scalar. The extension consists in replacing the overall continuous amount of vapor by its distribution into bins of different sizes. Therefore, the total amount of vapor void fraction predicted by the polydisperse model should approximate the vapor void fraction predicted by the model of Brandao and Mahesh (2022). The source term used for the main problem (Eqs. (5) and (6)), however, cannot be employed in this comparison since it needs information about the bubble radius and the bubble number density. Therefore, for this verification, we employ a source term that depends only on the void fraction and pressure difference, and was developed by Saito et al. (2007). The source term is then written as

$$\bar{S}_k = \dot{m}_{k-1/2} - \dot{m}_{k+1/2} + \dot{m}_k, \tag{A.1}$$

where

$$\begin{aligned}
\dot{m}_{k-1/2} &= C_e \bar{\alpha}_{k-1}^2 \bar{\alpha}_k^2 \frac{\rho_l}{\rho_v} \frac{max(p_v - \bar{p}, 0)}{\sqrt{2\pi R_v T}} - C_c \bar{\alpha}_{k-1}^2 \bar{\alpha}_k^2 \frac{max(\bar{p} - p_v, 0)}{\sqrt{2\pi R_v T}}, \\
\dot{m}_{k+1/2} &= C_e \bar{\alpha}_{k+1}^2 \bar{\alpha}_k^2 \frac{\rho_l}{\rho_v} \frac{max(p_v - \bar{p}, 0)}{\sqrt{2\pi R_v T}} - C_c \bar{\alpha}_{k+1}^2 \bar{\alpha}_k^2 \frac{max(\bar{p} - p_v, 0)}{\sqrt{2\pi R_v T}}, \\
\dot{m}_k &= C_e \bar{\alpha}_l^2 \bar{\alpha}_k^2 \frac{\rho_l}{\rho_v} \frac{max(p_v - \bar{p}, 0)}{\sqrt{2\pi R_v T}} - C_c \bar{\alpha}_l^2 \bar{\alpha}_k^2 \frac{max(\bar{p} - p_v, 0)}{\sqrt{2\pi R_v T}}.
\end{aligned} \tag{A.2}$$

Here, the term $\dot{m}_k$ is added such that the sum of the source term over all the bins is equal to the expression used in the work of Brandao and Mahesh (2022). The term α_l is the liquid volume fraction ($\alpha_l = 1 - \sum_{k=1}^{M} \alpha_k$).

The problem used for the validation here is different from the main problem investigated in this manuscript to lower computational costs. This simple problem is taken to be a flow over a circular cylinder under incipient conditions at low Reynolds number ($Re = 200$ based on cylinder diameter) and at $\sigma = 1.5$. This canonical problem has been investigated before in large-scale cavitation regimes (Gnanaskandan and Mahesh, 2016; Brandao et al., 2020). The cylinder is placed at the center of a $40 \times 20 \times 1$ rectangular computational domain, as given in Fig. A.33(*a*). The mesh spacing considered near the cylinder surface is $0.02D$ in both radial and azimuthal directions, which stretches further away. No-slip boundary conditions are applied to the bottom and top walls of the domain, while the spanwise walls have periodic boundary conditions. The very low Re used in this comparison results in a two-dimensional flow, thus 3 points are used in the spanwise direction. Here we compare the solutions obtained when the polydisperse model is used (Eq. (5)) and when it is not used (Eq. (2)). A total of 8 bins are used to represent bubbles of sizes ranging from 0.5 μm to 5 mm. The vapor distribution at the inflow is taken to be that of the seeded case (Fig. 3), which adds up to a total vapor volume fraction of 1.85×10^{-4}. Figs. A.33(*b*) and A.33(*c*) show mean total void fraction contours when the polydisperse model is used and when it is not used, respectively, and Fig. A.34 shows mean and fluctuation values of volume fraction across the wake centerline. It can be seen that, overall, the solution obtained with the polydisperse model has a good agreement with the solution obtained with the other model (Eq. (2)). However, it predicts a slightly smaller amount of total vapor.

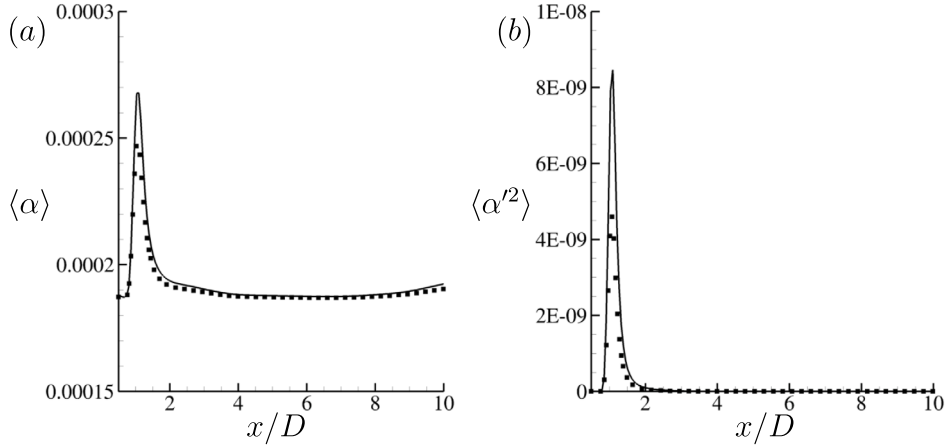

Fig. A.34. Profiles of $\langle\alpha\rangle$ (*a*) and $\langle\alpha'^2\rangle$ (*b*) when the polydisperse model is used (symbols) and when it is not used (lines).

References

Agarwal, K., Ram, O., Katz, J., 2018. Cavitating structures at inception in turbulent shear flow. In: Proceedings of the 10th International Symposium on Cavitation. CAV2018.

Amini, A., Seo, J., Rhee, S.H., Farhat, M., 2019. Mitigating tip vortex cavitation by a flexible trailing thread. Phys. Fluids 31 (12), 127103.

Arndt, R.E.A., 2002. Cavitation in vortical flows. Annu. Rev. Fluid Mech. 34 (1), 143–175.

Arndt, R.E.A., Arakeri, V.H., Higuchi, H., 1991. Some observations of tip–vortex cavitation. J. Fluid Mech. 229, 269–289.

Arndt, R.E.A., Keller, A.P., 1992. Water quality effects on cavitation inception in a trailing vortex. J. Fluids Eng. 114, 430–438.

Arndt, R.E.A., Maines, B.H., 2000. Nucleation and bubble dynamics in vortical flows. J. Fluids Eng. 122, 488–493.

Asnaghi, A., Bensow, R., Svennberg, U., 2017. Implicit large eddy simulation of tip vortex on an elliptical foil. In: Fifth International Symposium on Marine Propulsion.

Asnaghi, A., Svennberg, U., Bensow, R.E., 2020. Large eddy simulations of cavitating tip vortex flows. Ocean Eng. 195, 106703.

Astolfi, J.A., Fruman, D.H., Billard, J.Y., 1999. A model for tip vortex roll–up in the near field region of three–dimensional foils and the prediction of cavitation onset. Eur. J. Mech. B Fluids 18 (4), 757–775.

Bappy, M.H., Carrica, P.M., Li, J., Martin, J.E., Vela-Martin, A., Freire, L.S., Buscaglia, G.C., 2022. A sub-grid scale cavitation inception model. Phys. Fluids 34 (3), 033308.

Batchelor, G.K., 1964. Axial flow in trailing line vortices. J. Fluid Mech. 20 (4), 645–658.

Billet, M.L., Holl, J.W., 1981. Scale effects on various types of limited cavitation. J. Fluids Eng. 103 (3), 405–414.

Boulon, O., Callenaere, M., Franc, J.-P., Michel, J.-M., 1999. An experimental insight into the effect of confinement on tip vortex cavitation of an elliptical hydrofoil. J. Fluid Mech. 390, 1–23.

Brandao, F.L., Bhatt, M., Mahesh, K., 2020. Numerical study of cavitation regimes in flow over a circular cylinder. J. Fluid Mech. 885, A19.

Brandao, F.L., Mahesh, K., 2022. Large–eddy simulation of cavitation inception in a shear flow. Int. J. Multiph. Flow 146, 103865.

Cantwell, B.J., 1992. Exact solution of a restricted Euler equation for the velocity gradient tensor. Phys. Fluids A 4 (4), 782–793.

Chen, L., Zhang, L., Peng, X., Shao, X., 2019. Influence of water quality on the tip vortex cavitation inception. Phys. Fluids 31 (2), 023303.

Cheng, H., Long, X., Ji, B., Peng, X., Farhat, M., 2021. A new Euler–Lagrangian cavitation model for tip–vortex cavitation with the effect of non–condensable gas. Int. J. Multiph. Flow 134, 103441.

Chong, M.S., Perry, A.E., Cantwell, B.J., 1990. A general classification of three–dimensional flow fields. Phys. Fluids A 2 (5), 765–777.

da Silva, C., Pereira, C., 2008. Invariants of the velocity-gradient, rate–of–strain and rate–of–rotation tensors across the turbulent/nonturbulent interface in jets. Phys. Fluids 20 (5), 055101.

Fruman, D.H., Cerrutti, P., Pichon, T., Dupont, P., 1995. Effect of hydrofoil planform on tip vortex roll–up and cavitation. J. Fluid Eng. 117 (1), 162–169.

Germano, M., Piomelli, U., Moin, P., Cabot, W.H., 1991. A dynamic subgrid–scale eddy viscosity model. Phys. Fluids A 3:7, 1760.

Gnanaskandan, A., Mahesh, K., 2016. Numerical investigation of near–wake characteristics of cavitating flow over a circular cylinder. J. Fluid Mech. 790, 453–491.

Hsiao, C.-T., Chahine, G.L., 2005. Scaling of tip vortex cavitation inception noise with a bubble dynamics model accounting for nuclei size distribution. J. Fluids Eng. 127 (1), 55–65.

Hsiao, C.-T., Chahine, G.L., Liu, H.-L., 2003. Scaling effect on prediction of cavitation inception in a line vortex flow. J. Fluids Eng. 125, 53–60.

Jang, H., Mahesh, K., 2013. Large eddy simulation of flow around a reverse rotating propeller. J. Fluid Mech. 729, 151–179.

Jang, H., Verma, A., Mahesh, K., 2012. Predicting unsteady loads in marine propulsor crashback using large eddy simulation. Int. J. Rotating Mach. 2012.

Jeong, J., Hussain, F., 1995. On the identification of a vortex. J. Fluid Mech. 285, 69–94.

Khoo, M.T., Venning, J.A., Pearce, B.W., Brandner, P.A., 2020a. Nucleation effects on tip vortex cavitation inception location. In: 22nd Australasian Fluid Mechanics Conference. AFMC2020.

Khoo, M.T., Venning, J.A., Pearce, B.W., Brandner, P.A., 2020b. Statistical aspects of tip vortex cavitation inception and desinence in a nuclei deplete flow. Exp. Fluids 61 (145).

Khoo, M.T., Venning, J.A., Pearce, B.W., Takahashi, K., Mori, T., Brandner, P.A., 2020c. Natural nuclei population dynamics in cavitation tunnels. Exp. Fluids 61 (2), 1–20.

Kumar, P., Mahesh, K., 2017. Large eddy simulation of propeller wake instabilities. J. Fluid Mech. 814, 361–396.

Kumar, P., Mahesh, K., 2018. Large–eddy simulation of flow over an axisymmetric body of revolution. J. Fluid Mech. 853, 537–563.

Li, J., Carrica, P., 2021. A population balance cavitation model. Int. J. Multiph. Flow 138, 103617.

Lilly, D.K., 1992. A proposed modification of the Germano subgrid–scale closure model. Phys. Fluids A 4:3, 633–635.

Mahesh, K., Constantinescu, G., Moin, P., 2004. A numerical method for large–eddy simulation in complex geometries. J. Comput. Phys. 197:1, 215–240.

Mahesh, K., Kumar, P., Gnanaskandan, A., Nitzkorski, Z., 2015. LES applied to ship research. J. Ship Res. 59 (4), 238–245.

McCormick, Jr., B.W., 1962. On cavitation produced by a vortex trailing from a lifting surface. J. Basic Eng. 369–379.

Moore, D.W., 1974. A numerical study of the roll–up of a finite vortex sheet. J. Fluid Mech. 63 (02), 225–235.

Ooi, A., Martin, J., Soria, J., Chong, M., 1999. A study of the evolution and characteristics of the invariants of the velocity–gradient tensor in isotropic turbulence. J. Fluid Mech. 381, 141–174.

Park, N., Mahesh, K., 2009. Reduction of the Germano–identity error in the dynamic Smagorinsky model. Physics of Fluids (1994-present) 21 (6), 065106.

Park, K., Seol, H., Choi, W., Lee, S., 2009. Numerical prediction of tip vortex cavitation behavior and noise considering nuclei size and distribution. Appl. Acoust. 70, 674–680.

Perry, A.E., Chong, M.S., 1994. Topology of flow patterns in vortex motions and turbulence. Appl. Sci. Res. 53, 357–374.

Pichon, T., Pauchet, A., Astolfi, A., Fruman, D.H., Billard, J.Y., 1997. Effect of tripping laminar–to–turbulent boundary layer transition on tip vortex cavitation. J. Ship Res. 41 (1), 1–9.

Saito, Y., Takami, R., Nakamori, I., Ikohagi, T., 2007. Numerical analysis of unsteady behavior of cloud cavitation around a NACA0015 foil. Comp. Mech 40, 85–96.

Shin, S., Hong, J., Nagarathinam, D., Ahn, B.K., Park, S.G., 2021. Tip vortex cavitation and induced noise characteristics of hydrofoils.. Appl. Sci. 11, 5906.

Truesdell, C., 1954. The Kinematics of Vorticity, first ed. Indiana University Press.

Verma, A., Jang, H., Mahesh, K., 2012. The effect of an upstream hull on a propeller in reverse rotation. J. Fluid Mech. 704, 61–88.

Verma, A., Mahesh, K., 2012. A Lagrangian subgrid–scale model with dynamic estimation of Lagrangian time scale for large eddy simulation of complex flows. Phys. Fluids 24 (8), 085101.

Xie, C., Liu, J., Jiang, J.W., Huang, W.X., 2021. Numerical study on wetted and cavitating tip–vortical flows around an elliptical hydrofoil: Interplay of cavitation, vortices, and turbulence. Phys. Fluids 33 (9), 093316.

You, D., Wang, M., Moin, P., Mittal, R., 2006. Effects of tip–gap size on the tip–leakage flow in a turbomachinery cascade. Phys. Fluids 18 (10), 105102.